Remote Sensing of Environment 301 (2024) 113943

Contents lists available at ScienceDirect

Remote Sensing of Environment

journal homepage: www.elsevier.com/locate/rse

A hyperspectral view of the nearshore Mississippi River Delta: Characterizing suspended particles in coastal wetlands using imaging spectroscopy

Joshua P. Harringmeyer [a,*], Nilotpal Ghosh [a], Matthew W. Weiser [a], David R. Thompson [b], Marc Simard [b], Steven E. Lohrenz [c], Cédric G. Fichot [a,*]

[a] Boston University Department of Earth and Environment, Boston, MA, USA
[b] Jet Propulsion Laboratory, California Institute of Technology, Pasadena, CA, USA
[c] School for Marine Science and Technology, University of Massachusetts Dartmouth, New Bedford, MA, USA

ARTICLE INFO

Edited by: Menghua Wang

Keywords:
Suspended sediment
Imaging spectroscopy
Hyperspectral
Particulate organic carbon (POC)
River delta
Coastal ocean

ABSTRACT

Suspended particle concentration (Total Suspended Solids or TSS) determines sediment availability for deposition, whereas particle physico-chemical properties (e.g. composition and size) can influence sediment transport and accretion. These variables are critical to modeling and understanding nearshore sediment dynamics and coastal soil accretion and erosion. Upcoming satellite imaging spectrometers (e.g., GLIMR, SBG) have the potential to improve the detailed mapping and characterization of suspended particles in nearshore areas. Here, we conducted a detailed feasibility study assessing the capacity of imaging spectroscopy to accurately map suspended particle concentrations and physico-chemical properties in the Mississippi River Deltaic Plain (Louisiana, USA), a nearshore system with extreme coastline vulnerability. To that end, a large dataset of in situ TSS, Particulate Organic Carbon (POC) concentration, particle size, inherent optical properties (IOPs), and hyperspectral remote sensing reflectance (R_{rs}) was collected during the 2021 NASA Delta-X field campaigns in coastal Louisiana. Analyses of the data revealed that the enhanced spectral information provided by imaging spectroscopy (hyperspectral R_{rs}) improved the retrieval of TSS and POC/TSS (% organic carbon content), but highlighted the challenge of retrieving particle size in this system. Partial-least-squares-regression (PLSR) algorithms for TSS performed better than existing state-of-the-art algorithms and confirmed the importance of using local measurements and near-infrared R_{rs}. Implementation on Airborne Visible Infrared Imaging Spectrometer-Next Generation (AVIRIS-NG) imagery generated high-resolution (< 5 m), high-quality maps of TSS and POC/TSS in contrasted areas with a wide range of TSS concentrations from (0.1 to 100 mg L^{-1}), and demonstrated the enhanced potential of upcoming missions such as SBG and GLIMR to inform studies of nearshore sediment dynamics and coastal vulnerability/resilience.

1. Introduction

River deltas and coastal wetlands are under severe threat from subsidence and erosion, intensified by sea level rise and sediment starvation from upstream damming and channelization (Giosan et al., 2014; Saintilan et al., 2022; Törnqvist et al., 2020). Predicting the response of vulnerable coastlines to environmental change is increasingly critical, as changes in ecosystem health, water quality, and land loss have devastating effects on local economies and public health (Barbier et al., 2011; Costanza et al., 2014). The concentration of total suspended solids (TSS, mg of particles per liter of water) is a crucial water quality parameter to local stakeholders for monitoring water quality (Bilotta and Brazier, 2008), understanding changes in coastal erosion or accretion processes (Blum and Roberts, 2009), and for predicting coastline stability (Liu et al., 2021a). TSS indicates sediment availability, and its monitoring in nearshore systems can help understand changes in coastal erosion or accretion processes. The vulnerable coastline of the Mississippi River Deltaic Plain, the largest river system in North America, is a national hub of transportation infrastructure with critical ecosystems and natural resources (Twilley et al., 2016). Decreased sediment availability,

* Corresponding authors.
E-mail addresses: joshuaph@bu.edu (J.P. Harringmeyer), cgfichot@bu.edu (C.G. Fichot).

https://doi.org/10.1016/j.rse.2023.113943
Received 4 July 2023; Received in revised form 7 November 2023; Accepted 28 November 2023
Available online 14 December 2023

declining accretion, subsidence, and erosion all threaten the stability of coastlines in the Mississippi River Deltaic Plain (Syvitski et al., 2009), which are rapidly losing ground.

In the Mississippi River Deltaic Plain and in most nearshore waters, TSS concentration alone does not fully describe sediment availability, as particles with mineral, detrital organic, and algal sources occur across a wide range of sizes, chemical composition, and densities (Bianchi et al., 2011; Wang et al., 2004). These characteristics also influence the transportation, accretion, and fate of suspended particles (Edmonds et al., 2010). Particulate organic carbon (POC) is a biogeochemical parameter representing the organic content of sediment load. The mass-fraction of particles composed of organic carbon, derived by normalizing POC by TSS (POC/TSS), is an important compositional indicator that influences particle density (Schartau et al., 2019) and therefore transport. Particles with high POC/TSS contribute less to accretion after deposition, as organic matter in the particles can be removed through mineralization. Variability in POC/TSS also impacts the sequestration of terrigenous (non-algal) organic matter, an important ecosystem service provided by coastal estuary systems (Galy et al., 2015; Goñi et al., 1998; Hedges et al., 2001). Particle size also affects sediment fate. In particular, flocculation and aggregation are common in estuarine systems and can reduce sediment transport (Khelifa and Hill, 2006), as large diameter particles have higher settling velocities and are transported shorter distances.

In situ measurements of TSS concentration and properties can help quantify suspended particles dynamics and assess the vulnerability of coastal systems. However, the dynamic and heterogenous nature of nearshore coastal ecosystems and the practical limitations of laboratory-based measurements make it difficult to characterize representative nearshore particle dynamics using these measurements alone (Cortese et al., 2023; Fichot et al., 2016; Pavelsky and Smith, 2009). River discharge, which delivers suspended sediment to the coastal ocean through estuaries and deltas, is often highest during spring months in temperate systems (Allison et al., 2012; Zhang et al., 2020). Suspended particles from sediment resuspension and/or phytoplankton production also contribute to ambient TSS in these systems (Bianchi et al., 2007; Boss et al., 2001; Sweet et al., 2022). These sources vary with seasons and episodic events caused by wind waves, runoff, tides, changing water level, and other factors (Cortese and Fagherazzi, 2022; Kolker et al., 2014; Perez et al., 2000). Remote sensing can help to capture variability in TSS and particle properties driven by these processes in nearshore environments by providing regional snapshots at high spatial resolution.

However, approaches for accurately retrieving TSS and other in-water constituents in optically complex waters are still developing (Dierssen et al., 2021). Nearshore waters typically contain diverse optically active water constituents with varying properties (Mouw et al., 2015; Sathyendranath, 2000). Separating their optical influences is critical to retrieve particle concentration and properties accurately. Recent approaches have improved coastal and inland TSS retrieval (Balasubramanian et al., 2020; Jiang et al., 2021), but are designed for multispectral sensors, which are limited in their ability to separate and characterize constituents by the small number of spectral bands (Aurin and Dierssen, 2012). Particle carbon content has been retrieved remotely by harnessing the influence of POC/TSS on particle scattering properties (Stramski et al., 2007; Woźniak et al., 2010) and spectral absorption characteristics (Boss et al., 2018). However, these spectral signals can be subtle. Approaches to retrieve POC and POC/TSS exist (Evers-King et al., 2017; Liu et al., 2021b; Stramski et al., 2022; Tran et al., 2019), but they are mostly applicable to marine coastal waters where POC occurs at lower concentrations and is well-correlated with either TSS or chlorophyll-a concentration (Le et al., 2017; Son et al., 2009; Woźniak et al., 2016). A few studies have attempted to retrieve POC in similarly turbid natural waters (Lin et al., 2018; Lyu et al., 2017; Pan et al., 2023; Xu et al., 2020) to those encountered in the nearshore coastal Mississippi River Delta. These retrievals are often designed for inland waters and do not attempt to retrieve the POC/TSS ratio in such turbid waters. Similarly, remote sensing of particle size has been primarily conducted for oceanic waters (Kostadinov et al., 2009), although the same algorithms have also been applied to turbid waters, albeit without validation (e.g., Shi and Wang, 2019).

Ultraviolet (UV)–visible–near infrared (NIR) imaging spectroscopy (hyperspectral imagery) is expected to provide useful spectral information to separate the overlapping optical influences of in-water constituents and allow retrieval of biogeochemical and physical properties in coastal waters (Mouw et al., 2015; Werdell et al., 2018). A new generation of spaceborne sensors promise unprecedented observations of nearshore and inland waters such as the existing NASA Earth surface Mineral dust source InvesTigation (EMIT), the DLR Earth Sensing Imaging Spectrometer (DESIS), and the ASI PRecursore IperSpettrale della Missione Applicativa (PRISMA); as well as the upcoming NASA Geostationary Littoral Imaging and Monitoring Radiometer (GLIMR) and Surface Biology and Geology (SBG) missions, and the upcoming ESA Copernicus Hyperspectral Imaging Mission for the Environment (CHIME). Established airborne instruments, such as the NASA Portable Remote Imaging SpectroMeter (PRISM, ~2.8 nm spectral sampling) or the Airborne Visible/Infrared Imaging Spectrometer-Next Generation (AVIRIS-NG, ~5 nm spectral sampling) provide imaging spectroscopy at very high spatial resolution (variable spatial sampling, as fine as a few meters), albeit for more limited spatial extent (Chapman et al., 2019). Airborne imaging spectroscopy can be useful for applications requiring the resolution of small features (e.g., narrow channels) and provide a test case for developing algorithms applicable to future satellite missions (Candela et al., 2021; Dierssen et al., 2015, 2021; Fichot et al., 2016; Harringmeyer et al., 2021).

Here, we assess utility of imaging spectroscopy for mapping TSS and particle properties in coastal wetland waters of Louisiana using two primary criteria:

1. TSS concentration and properties should be retrieved accurately across a wide range of concentrations (tested here on 10^{-1} to 10^{2} mg L^{-1}) and improve upon existing approaches,
2. Mapped TSS concentration and properties should resolve real spatial features and temporal variability that are largely free of artifacts.

In situ and airborne measurements collected during the 2021 NASA Earth Venture Suborbital (EVS)-3 Delta-X field campaigns in coastal Louisiana were used to examine the relationships between particle concentration/properties and inherent optical properties (IOPs) to assess the feasibility of remote retrieval. These data were also used to develop and validate visible-NIR algorithms for retrieving TSS and POC/TSS. These algorithms were compared to existing approaches and applied to AVIRIS-NG imagery (Chapman et al., 2019) to capture the seasonal and spatial variability of suspended particles in Louisiana marsh-estuary waters. This study provides a robust test case for nearshore suspended particle characterization from remote sensing considering: 1. the unusually wide concentration range and diversity of suspended particles (e.g., terrigenous, autochthonous, inorganic, organic), 2. the large dataset of collocated field and airborne measurements aiding in algorithm validation, and 3. the collection of high-quality AVIRIS-NG imagery over nearshore waters. We analyzed the spatiotemporal variability of TSS concentration and carbon content and evaluated maps for their ability to resolve spatial features indicative of the hydrodynamic conditions and sediment sourcing. Finally, we evaluated the impact of optically shallow water and adjacency effects on TSS retrieval on products in the nearshore coastal zone.

2. Data and methods

Delta-X field data and airborne imagery were collected in spring and fall 2021. Field sampling included: 1. collection of water samples for laboratory analysis of TSS and POC concentration, 2. in situ measurements of particulate backscattering (b_{bp}), turbidity, particle size,

Table 1
Summary of field water-quality measurements. Parameter ranges are reported for each campaign, with the median in parentheses.

Campaign	Basin	Salinity [PSU]	Temperature [°C]	Total Suspended Solids (TSS) [mg L^{-1}]	Turbidity [FNU]	b_{bp}(440) [m^{-1}]	POC [mg L^{-1}]	POC/TSS [%]	Sauter Mean Diameter [μm]
GulfCarbon 2009–2010	Northern Gulf of Mexico ocean margin	23.1–36.6 (34.1)	15.3–23.1 (23.3)	0.09–8.63 (0.785)	–	0.002–0.086 (0.009)	–	–	–
Delta-X Spring 2021	Atchafalaya	0.1–0.28 (0.14)	15.2–21.6 (15.8)	16.2–154.5 (79.7)	11.1–72.8 (47.9)	0.324–1.78 (1.18)	0.544–2.82 (1.79)	1.44–6.16 (2.21)	13.7–50.8 (26.4)
	Terrebonne	0.14–25.7 (7.1)	18.1–26.0 (20.9)	2.2–90.1 (32.6)	0.76–50.8 (17.4)	0.221–1.30 (0.416)	0.309–4.25 (1.69)	1.84–18.4 (4.01)	10.9–74.1 (41.0)
Delta-X Fall 2021	Atchafalaya	0.16–0.22 (0.20)	26.4–31.8 (30.9)	13.4–35.0 (20.8)	8.36–19.6 (11.9)	0.237–0.471 (0.318)	0.532–2.10 (0.803)	2.19–8.88 (3.50)	12.9–69.3 (35.4)
	Terrebonne	0.13–22.1 (6.01)	24.8–32.8 (29.8)	6.58–68.9 (21.4)	3.07–54.8 (11.1)	0.0631–0.957 (0.256)	0.683–4.86 (2.36)	3.18–23.2 (11.1)	13.4–70.3 (29.6)

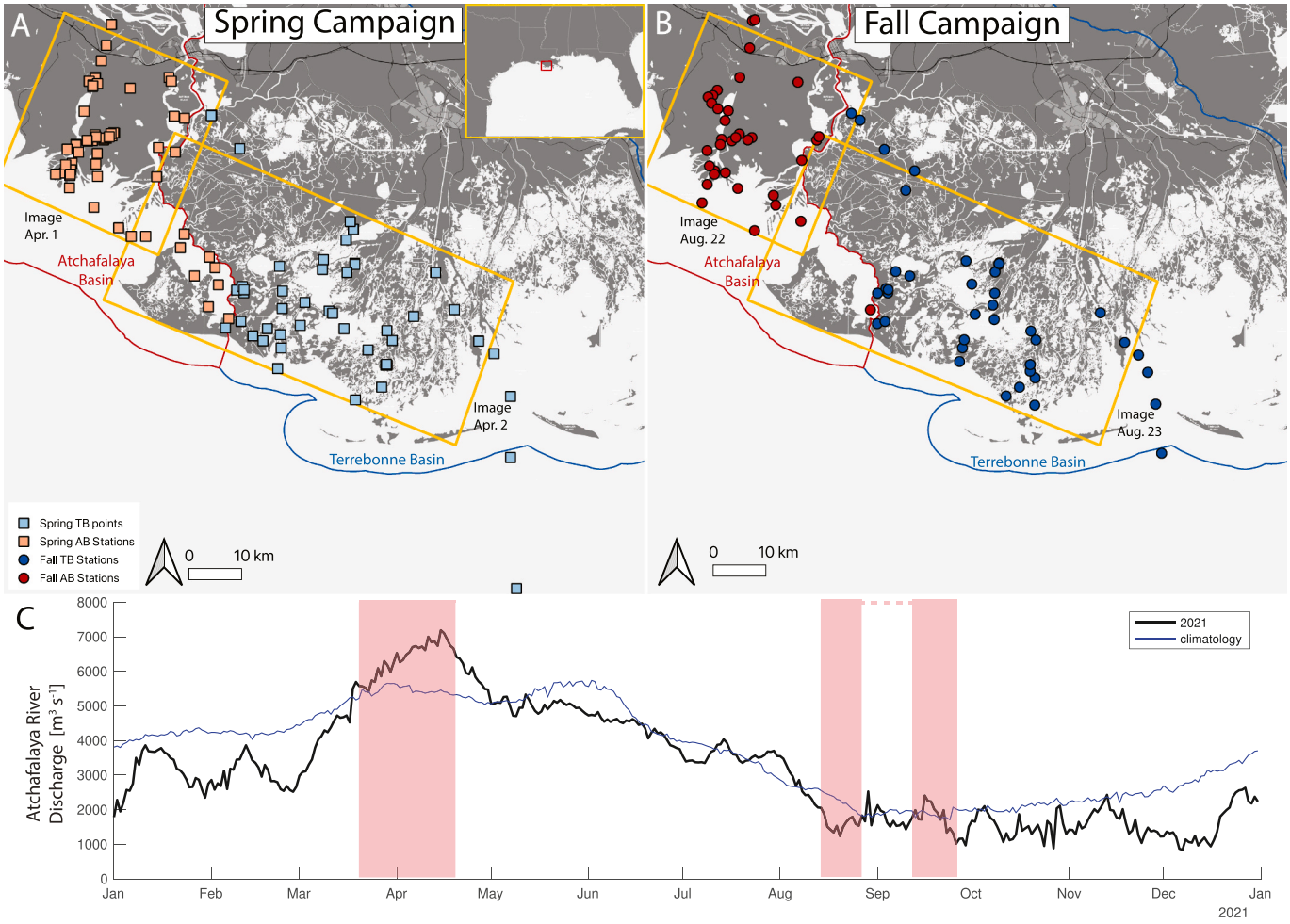

Fig. 1. Study area in coastal Louisiana, USA, with field sampling stations, sampling periods, and corresponding river discharge. (A) Spring 2021 field campaign samples were collected between March 26–April 22, 2021, and (B) Fall 2021 field campaign samples were collected between August 14–September 24, 2021. Data were divided by basin between the river-influenced, aggrading Atchafalaya Basin to the west (red outline), and the marsh-dominated, eroding Terrebonne Basin to the east (blue outline). Yellow boxes outline approximate AVIRIS-NG image mosaic extents. Field sampling campaigns were scheduled to measure conditions during seasonal high and low river discharge, shown (C) at the USGS Atchafalaya River gauge at Morgan City, LA for 2021 (black) and the corresponding daily climatology for 1995–2022 (blue). The sampling periods are shaded in red on the discharge plot. (For interpretation of the references to colour in this figure legend, the reader is referred to the web version of this article.)

salinity, water temperature, and 3. in situ measurements of remote-sensing reflectance (R_{rs}). Field data from GulfCarbon research cruises, January 2009–March 2010, are used as a complementary data set for the TSS algorithm development and validation (Appendix A1).

2.1. Delta-X study area and field sampling

Field sampling was conducted at 192 stations in the Mississippi River Deltaic Plain in coastal Louisiana, USA (Table 1, Fig. 1A–B). The Mississippi River Deltaic Plain is an economically vital region under threat from coastline erosion, subsidence, and loss of upriver sediment inputs.

Understanding the stability of this coastline is critical, as the loss of vital coastal ecosystems threatens communities across the Gulf Coast and has economic impacts across the United States (Syvitski et al., 2009). The sampling region is located approximately 100 km west of the main birdsfoot delta of the Mississippi River and includes the river-influenced, aggrading Atchafalaya Basin and the marsh-dominated, eroding Terrebonne Basin (Fig. 1). Sediment concentration varies seasonally, correlated with discharge from the Atchafalaya River, which peaks during spring freshet. These basins demonstrate potential futures for the Mississippi River Deltaic Plain, as the Atchafalaya Basin is gaining land area, sustained by sediment inputs from the Atchafalaya River, while the Terrebonne Basin is losing land area without similar inputs (Allison et al., 2012; Twilley et al., 2016). The two basins contain a wide variety of particle types, which affect potential sediment accretion and subsidence in the region.

Field measurements were collected across a range of settings from small channels in forested and wetland areas to open-water bays and the nearshore continental shelf (salinity range 0.1–25.7 PSU). Spring field sampling was conducted between March 26–April 22, 2021, and fall sampling was conducted between August 14–25 and September 13–24, 2021. Spring and fall sampling were conducted during seasonal high and low Atchafalaya River discharge outflow respectively (Fig. 1C). Field sampling was halted from August 26–September 13, 2021, because of the landfall of a destructive storm (US Hurricane Irma) in Louisiana on August 29, 2021. Water quality was expected to have returned to background conditions by the time sampling continued, and ranges of measured constituents were consistent before and after the storm.

2.1.1. Total suspended solids (TSS) concentrations

Laboratory measurements of TSS (Fichot et al., 2022a) were conducted using a gravimetric method (Neukermans et al., 2012b). Surface water samples (~ 0.5 m depth) were collected using a 4-L Van Dorn sampler, and the entire sampled volume was immediately transferred to a 4-L amber polyethylene bottle and stored at 4 °C. Triplicate subsamples were filtered (after gently inverting the bottle to resuspend settled particles) through pre-weighed 47-mm glass-fiber filters (GFF, nominal pore size 0.7 μm). Filtered volumes (generally 100–500 mL) were selected using field-measured turbidity to maximize the mass of solids retained while avoiding clogging. Filters were dried at 75 °C for 24 h and allowed to cool to room temperature in a desiccator before being re-weighed (Sartorius AG Cubis Microbalance, μg precision). TSS was calculated as the increase in filter mass, divided by the volume of water filtered. Variability between triplicate TSS measurements was used to compute standard deviation.

2.1.2. Particulate Organic Carbon (POC) concentrations

Laboratory measurements of POC (Fichot et al., 2022b) were conducted on a Costech ECS 4010 CHNS Element Analyzer (EA), following the IOCCG protocol (Chaves et al., 2021). Surface water samples (~ 0.5 m depth) were collected using a 4-L Van Dorn sampler, and the entire sampled volume was immediately transferred to a 4-L amber polyethylene bottle and stored at 4 °C. Triplicate subsamples were filtered (after inverting the bottle to resuspend settled particles) through pre-weighed 25-mm GFF (nominal pore size 0.7 μm), and suspended particles were retained on the filter. Sample blanks were prepared from the filtrate of each sample that were separately filtered through a 47-mm GFF (0.7 μm pore size). All filters were folded in half, wrapped in pre-combusted aluminum foil, and stored in a freezer (−20 °C). Prior to sample processing and analyses, filters were thawed at 60 °C for 24 h in pre-furnaced, covered glass petri dishes before unwrapping them from the foil. To remove any inorganic carbon from the samples, the filters were opened in uncovered petri dishes and transferred to a glass desiccator containing concentrated Hydrochloric acid (ACS Plus HCl; Fisher Chemical #A144C-212) for 24 h. Acidified filters were dried in a dedicated oven for 24 h at 60 °C before being pelletized in tin (Sn) capsules for analysis on the EA. Calibration was performed by running a range of atropine standards (~0.02–0.20 mg C). An analytical blank (furnaced 25-mm GFF) and unknown mass of atropine was run as a check standard between each set (sample blanks and replicates) for instrument drift while NIST Buffalo River Sediment (RM 8704) was analyzed to check for consistency between runs. POC concentration (mg L^{-1}) was calculated as the blank-corrected measured carbon mass retained on the filter (mg) divided by the volume of water filtered. The triplicate measurements were used to compute standard deviation.

2.1.3. Remote-sensing reflectance spectra

R_{rs} was measured in situ (Fichot and Harringmeyer, 2022a) using an above-water approach adapted from the protocol described by Mobley (Mobley, 1999, 2015). A Spectral Evolution handheld Portable SpectroRadiometer (PSR-1100f) was used to measure calibrated, dark-corrected radiance from three targets:

1. from a reflective (> 99% reflectance) Spectralon® Lambertian panel, at 40° from nadir and 135° azimuth from the solar principal plane;
2. from the sky, at 40° from zenith and 135° azimuth from the solar principal plane;
3. from the water, measuring total upwelling radiance, at 40° from nadir and 135° azimuth from the solar principal plane.

Each target was measured 4–6 times over 1–2 min to minimize the influence of changing conditions (e.g., moving clouds or variable wind). The sequence of targets was repeated 2–3 times to maximize the number of measurements for estimating uncertainty. Care was taken to maintain viewing geometry and to minimize the influence of shading or light reflected from the boat. R_{rs}(380–900 nm) spectra were estimated from the radiance measurements:

$$R_{rs}(\lambda) = \left(L_{water+sky}(\lambda) - \rho(\lambda) * L_{sky}(\lambda)\right) / \left(\pi * L_{panel}(\lambda) / R_{panel}(\lambda)\right) \quad (1)$$

where $L_{water+sky}$ is the total upwelling radiance, L_{sky} is the sky radiance, L_{panel} is radiance from the Lambertian panel, R_{panel} is the reference panel reflectance (approximately 99%; manufacturer-supplied spectral values used in the calculation), and λ refers to wavelength. The factor π is used for a hemispherical integration of L_{panel} to an equivalent downwelling irradiance assuming perfect Lambertian diffusion. The fraction of incident skylight reflected at the air-water interface, ρ, was estimated using the lookup tables of Zhang et al. (Zhang et al., 2017) using viewing geometry, field-measured wind speed, estimated cloud cover, an estimated aerosol optical depth of 0.2 for the spring campaign and 0.24 for the fall campaign, and solar zenith angle calculated from latitude, longitude, and time. This skylight correction differs slightly from the approach described in Fichot and Harringmeyer (2022a), which was calculated using the lookup tables of Mobley (2015). This change resulted in only small differences in the R_{rs} spectra. The spectra used in this work are available in the Suplementary material.

The median spectrum was taken for a series of measurements of single target (i.e., water, reflectance panel, or sky). Outlier spectra–spectra differing from the median spectrum by >3 median absolute deviations at more than one third of wavelengths—were removed. Median radiance spectra were then used to calculate R_{rs} for each series. This resulted in 2–3 R_{rs} spectra per station, one for each series of measurements collected at station. The mean of the 2–3 R_{rs} spectra was then calculated, and a Savitzky-Golay filter (frame size 13, polynomial order 4) was applied for spectral smoothing (Savitzky and Golay, 1964; Vandermeulen et al., 2017).

Finally, an empirical correction was applied to remove residual sun glint from reflectance measurements. This glint correction (Jiang et al., 2020) utilized the empirical relationship between a shoulder in the absorption spectrum of pure water (780–840 nm) and the magnitude of glint-free remote sensing reflectance at 810 nm to calculate a scalar correction factor that was subtracted from all wavelengths. For direct comparability to AVIRIS-NG spectra, field reflectance spectra were

interpolated from 1 nm spectral resolution to AVIRIS-NG band centers.

Measurement uncertainty was determined for R_{rs} by estimating individual sources of uncertainty and propagating error through the calculation. The standard deviation of the $L_{water+sky}(\lambda)$, $L_{panel}(\lambda)$, and $L_{sky}(\lambda)$ spectra and the manufacturer-supplied $R_{panel}(\lambda)$ uncertainty were propagated through the calculation of R_{rs}. Uncertainty in ρ was estimated by perturbing wind speed (uniform distribution from 0 to field-measured speed), view azimuth angle (135° ± 20°), and view zenith angle (40° ± 10°). The standard deviation of ρ under these perturbations was also propagated to calculate the uncertainty in $R_{rs}(\lambda)$ due to uncertainty in ρ.

A manual review was conducted to check for changing sky conditions or measurement of the incorrect target. In this step, normalized $L_{water+sky}(550)$, $L_{panel}(550)$, and $L_{sky}(550)$ from each measured spectrum were plotted, and series where $L(550)$ changed by >10% while measuring a single target were excluded from analysis (Supplementary Fig. S1).

2.1.4. In situ water-quality parameters

Water-quality indicators, including temperature, salinity, and turbidity (Fichot et al., 2022c) were measured in situ (~0.5 m depth) using either a Yellow Springs Instruments Inc. (YSI) ProDSS or a YSI EXO-3 multi-sensor water-quality instrument. Salinity was calibrated using a potassium chloride standard solution (10,000 μsiemens cm^{-1} at 25 °C). Turbidity was calibrated using a two-point, 0–124 Formazin Nephelometric Units (FNU) calibration curve between pure water (Millipore Milli-Q Direct 16) and a traceable polymer turbidity standard (YSI Inc.). Sampling station locations were determined using the on-board GPS of the YSI handheld unit.

2.1.5. Optical backscattering coefficients of suspended particles

In situ optical backscattering coefficient by particles (b_{bp}) at 440 nm and 700 nm was measured using an ECO BB2FL instrument (Sea-Bird Scientific). The methodology is described in detail in Appendix A2). Briefly, the intensity of light backscattered at 124° (Doxaran et al., 2016) was corrected for dark current and multiplied by a manufacturer-provided calibration factor to calculate volume scattering function (VSF) at 124° ($\beta_{raw}(124°, \lambda)$). This VSF was corrected for non-water absorption along the path as recommended by Doxaran et al. (2016). Non-water absorption was the sum of laboratory-measured absorption coefficient (Section 2.1.8) of suspended particles (a_p) and of chromophoric dissolved organic matter (a_g). The corrected VSF (β_{cor}) was used to calculate b_{bp} by subtracting the VSF at 124° for pure water:

$$b_{bp}(\lambda) = 2\pi\chi(\beta_{cor}(124°, \lambda) - \beta_w(124°, \lambda, S)) \quad (2)$$

where $b_{bp}(\lambda)$ is the particulate backscattering, $\chi = 1.1$ is a correction factor related to sensor scattering angle (Doxaran et al., 2016), and $\beta_w(\lambda, S)$ is the salinity-dependent VSF for brackish water (Zhang and Hu, 2009). At 85 stations, b_{bp} reached the saturation limit of the detector, so b_{bp} was estimated from field-measured turbidity. A linear relationship between turbidity and b_{bp}(440, 700) was estimated using data from stations where b_{bp} did not saturate (Appendix A2).

2.1.6. Mean suspended particle diameter and beam attenuation coefficient

In situ suspended particle size distribution was measured using a Sequoia Scientific, Laser In Situ Scattering and Transmissometer (LISST)-200X instrument (Fichot and Harringmeyer, 2022b). Beam attenuation and angular particle scattering at 670 nm were measured in surface waters (~0.5 m depth) at a rate of 1 Hz for approximately two minutes. Instrument calibration was maintained by collecting a new zero-scattering measurement on pure water (Millipore Milli-Q Direct 16) each day during field sampling. Beam attenuation coefficient ($c(670)$) and angularly binned particle scattering intensity at each station were processed using a manufacturer-provided MATLAB script for non-spherical particles to calculate the Sauter mean particle diameter, and volumetric particle concentration (volume of particles per liter of water), referred here to as volumetric TSS (μL L^{-1}). Particle apparent density (ρ_a, kg m^{-3}) was calculated by dividing laboratory-measured TSS (mg L^{-1}) by LISST-derived volumetric TSS (μL L^{-1}).

2.1.7. Particle and CDOM optical absorption coefficients

The absorption coefficients of particles and CDOM were measured using standard methods (Neeley and Mannino, 2018; Stramski et al., 2015), which are described in more detail in Appendix A3. Suspended particles were retained on a 25-mm GFF (nominal pore size 0.7 μm), and the absorption coefficient of particles was measured on a spectrophotometer using the inside-sphere method (Stramski et al., 2015). Samples filtered through a GFF (nominal pore size 0.7 μm) were measured for CDOM absorption coefficient using a dual-beam spectrophotometer.

2.2. Delta-X AVIRIS-NG imagery

The AVIRIS-NG sensor was deployed on a Dynamic Aviation King Air B200 aircraft on several days during both campaigns. Each flight line was collected over ~10 min. Imagery was collected at approximately 5-nm spectral sampling from 380–2500 nm and 3.8 to 5.4 m spatial sampling (Thompson et al., 2023). Imaging conditions were generally clear during the spring campaign, with low aerosol and water vapor loads. In contrast, most days during the fall campaign showed very high levels of atmospheric water vapor, reaching 5 g cm^{-2} during August. Surface reflectance spectra were calculated using an optimal estimation approach (ISOFIT package) that simultaneously estimates atmospheric and surface reflectance contributions to at-sensor radiance (Thompson et al., 2019). Vicarious sensor calibration, utilizing a near-simultaneous field R_{rs} spectrum, was applied to update the laboratory calibration. A bi-directional reflectance distribution function (BRDF) correction was applied to the AVIRIS-NG R_{rs} generating Level 2b products (Greenberg et al., 2022) and a glint correction was applied to open water pixels. A water mask was derived from band-ratio thresholds utilizing red, NIR, and SWIR R_{rs} (Greenberg et al., 2022). A cloud mask was derived from R_{rs} band thresholds on the AVIRIS-NG imagery (Jensen et al., 2019) (mask equations presented in Appendix A4). A 3 × 3 or 5 × 5 median-pixel filter was applied to remove "salt-and-pepper" artifacts (e.g., residual glint) in the retrieved products.

2.3. GulfCarbon field data

Measurements ($n = 66$) of TSS, R_{rs}, and b_{bp} were collected between January 2009 and March 2010 on the continental shelf and open-ocean waters of the Northern Gulf of Mexico (Salinity: 23.1–36.6 PSU). These previously published data (Chakraborty, 2013; Epps, 2018; Fichot et al., 2014; Verma et al., 2021) included surface waters with lower TSS concentrations than in the Delta-X dataset and facilitated the parameterization of the algorithms. Methods for gravimetric TSS, R_{rs} measured with a Sea-Bird Scientific HyperPro compact optical profiler, and b_{bp} measured with a Sea-Bird Scientific VSF3 are summarized in Appendix A1.

2.4. TSS algorithms

We developed a visible–NIR partial-least-squares regression (PLSR) algorithm and tested its performance against that of existing algorithms developed by Nechad et al. (2010), Jensen et al. (2019), Jiang et al. (2021), and an update to the Jiang et al. (2021) algorithm using local coefficients. We also assessed the potential capabilities of sensors with only visible bands by testing a PLSR utilizing only visible AVIRIS-NG wavelengths.

2.4.1. PLSR-based algorithms

Two log-log transformed PLSR-based approaches (*plsregress* MATLAB function) were developed using in situ TSS and R_{rs}: a Visible-NIR

Table 2
Jiang2021 algorithm wavelengths and backscattering vs. TSS equations. Local updates to these equations (*JiangUpdate*) were developed using the Delta-X and GulfCarbon in situ data.

Water Type	*Jiang2021*	*JiangUpdate*
Type I-Open Ocean	$TSS = 94.607 \times b_{bp}(560)$	$TSS = 79.18 \times b_{bp}(560) + 0.08201$
Type II-Coastal	$TSS = 114.012 \times b_{bp}(665)$	$TSS = 1.538\ e^{21.21 \times b_{bp}(665)} - 1.767\ e^{-127.0 \times b_{bp}(665)}$
Type III-Highly Turbid	$TSS = 137.665 \times b_{bp}(754)$	$TSS = 113.5 \times b_{bp}(754) - 2.229$
Type IV-Extremely Turbid	$TSS = 166.168 \times b_{bp}(865)$	$TSS = 154.2 \times b_{bp}(865) - 11.47$

approach (*Vis-NIR PLSR*) and a visible-only PLSR (*Vis-only PLSR*). PLSR is a well-suited approach for imaging spectroscopy because it reprojects many correlated predictor variables to estimate a smaller set of uncorrelated latent variables that predict the response variable. These latent variables correspond to major modes of variability in the predictors (R_{rs}) that are correlated with the response variable, preserving subtle features in the spectral shape that are correlated with the response variable (Wold et al., 2001). The resulting model retrieves TSS from R_{rs} using:

$$TSS = exp(\beta_0 + \beta_{\lambda 1} \times ln(R_{rs}(\lambda_1)) + \beta_{\lambda 2} \times ln(R_{rs}(\lambda_2)) \ldots + \beta_{\lambda i} \times ln(R_{rs}(\lambda_i)))) \quad (5)$$

where β_0 is an intercept and coefficients $\beta_{\lambda 1}$ to $\beta_{\lambda i}$ correspond to the AVIRIS-NG wavelengths.

A variable importance projection (VIP) (Farrés et al., 2015) variable reduction was implemented on the PLS regressions. Wavelengths with VIP scores >1 were included in the final algorithm, reducing the wavelengths used from 430–900 nm to 658–898 nm for the *Vis-NIR PLSR* algorithm, and from 430–723 nm to 602–723 nm for the *Vis-Only PLSR* algorithm. Seven latent variables were used for both PLSR algorithms, selected by increasing the number of latent variables until the mean absolute error (MAE) of the leave-one-out cross-validation no longer decreased with additional latent variables (Arlot and Celisse, 2010). Regression coefficients for implementing *Vis–NIR PLSR* and *Vis-Only PLSR* are presented in Supplementary Table ST1.

An algorithm for retrieving turbidity from R_{rs} was also developed using a log-log PLSR approach on Vis-NIR R_{rs}. This algorithm may be of use to end-users utilizing only a turbidity probe. Algorithm calibration, leave-one-out cross-validation and VIP variable reduction were conducted, resulting in an algorithm with 8 latent variables, on R_{rs}(718–898) (Supplementary Table ST2 and ST3 and Supplementary Fig. S2).

2.4.2. Nechad et al., 2010 Empirical algorithm

The Nechad et al. (2010) algorithm (*Nechad2010*) uses a non-linear relationship between R_{rs} and TSS at a user-selected wavelength λ_0 between 520 and 885 nm:

$$TSS = \frac{A^{\rho} \times \pi R_{rs}(\lambda_0)}{1 - \pi R_{rs}(\lambda_0)/C^{\rho}} + B^{\rho} \quad (6)$$

where A^{ρ}, B^{ρ}, and C^{ρ} are wavelength-specific, empirical constants calibrated using data collected in the North Sea. Nechad et al. reported optimal performance at $\lambda_0 = 712.5$ nm, so that wavelength was used here.

2.4.3. Jiang et al., 2021 Semi-empirical algorithm

The Jiang et al. (2021) algorithm (*Jiang2021*) uses two steps: 1. The QAA semi-analytical algorithm (Lee et al., 2007, 2014) is used to retrieve b_{bp} from R_{rs}, and 2. b_{bp} is converted to TSS using an empirical coefficient. In the first step, *Jiang2021* categorizes a spectrum into one of four water types based on reflectance band ratios (Type I. open ocean, Type II. coastal, Type III. highly turbid, and Type IV. extremely turbid). The algorithm utilizes longer wavelength R_{rs} and b_{bp} (red to near-Infrared) for more turbid waters. Backscattering is then multiplied by an empirical coefficient $\beta(\lambda)$ to retrieve TSS:

$$TSS = \beta(\lambda) \times b_{bp}(\lambda) \quad (7)$$

The coefficients, $\beta(\lambda)$, in *Jiang2021* (Table 2) were determined using a synthetic dataset created from bio-optical modeling across a range of chlorophyll (0.02–1000 mg m^{-3}) and detrital particle (0.02–1000 g m^{-3}) concentrations, $b_{bp}(\lambda)$ spectral slopes, and mass-specific-scattering values.

2.4.4. Jiang et al., 2021 Updated coefficients

We tested an update to *Jiang2021* (*JiangUpdate*) using locally calibrated relationships between $b_{bp}(\lambda)$ and TSS. The Delta-X (mostly Type III and IV) and GulfCarbon (mostly type I and II) data were classified into water types as in *Jiang2021*. Field measurements were used to derive local relationships between $b_{bp}(\lambda)$ and TSS, equivalent to $\beta(\lambda)$ in *Jiang2021*. We relaxed the *Jiang2021* assumption that TSS and $b_{bp}(\lambda)$ are related by a single constant, allowing for non-zero intercepts and non-linear fits (Table 2).

2.4.5. Jensen et al., 2019 PLSR algorithm

Jensen et al. (2019) developed a PLSR algorithm (*Jensen2019)* for AVIRIS-NG, using field data from a 2015 preliminary Delta-X field campaign. This algorithm provides two options for retrieval, either from R_{rs} or from the spectral derivative of R_{rs} (*dRrs*). Jensen et al. (2019) found that the dR_{rs}-based approach more accurately retrieved TSS. Applied to the Delta-X and GulfCarbon data, the R_{rs}-based approach better retrieved TSS, so that approach is used here. The nominal band-centers of the AVIRIS-NG instrument changed slightly during recalibration, so R_{rs} from the Delta-X campaign was linearly interpolated to the wavelengths used in *Jensen2019*.

2.5. POC/TSS PLSR algorithm

We developed a visible-NIR PLSR algorithm (*POC/TSS PLSR*) for retrieving particle carbon content from in situ POC/TSS and R_{rs}. The algorithm retrieves POC/TSS from R_{rs} using the same log-log approach as the TSS PLSR algorithms. Variable reduction using the VIP was implemented on the *POC/TSS PLSR* algorithm (Farrés et al., 2015), reducing the wavelengths used from 430–900 nm to 430–497 nm, 663–683 nm, 738–763 nm, and 823–900 nm. Seven latent variables minimized leave-one-out cross-validation MAE (Arlot and Celisse, 2010), and were used for the *POC/TSS PLSR* algorithm. The regression coefficients for implementing the *POC/TSS PLSR* algorithm are presented in Supplementary Table ST4.

2.6. Algorithm calibration and validation

A subset of field stations—comprising 10% of field sampling stations—was selected for independent validation of algorithm performance. The remaining 90% of the data was used to calibrate the PLSR algorithms. Stations selected for the Delta-X validation set covered the full range of TSS concentrations (validation sample locations and matchup image extents are presented in Supplementary Fig. S3). End-to-end validation was conducted by comparing algorithm performance using AVIRIS-NG spectra, the median from 3 × 3 square of pixels around the sampling station, collected within 3 h of field sampling. Spectra from these pixels met homogeneity requirements ($R_{rs}(\lambda)$ maximum coefficient of variation <0.3) for usability. The validation sets differed between in situ and AVIRIS-NG validation. The subset for in situ validation ($n = 21$ spectra, 15 Delta-X and 6 GulfCarbon stations) included stations from both Delta-X and GulfCarbon. The subset for the AVIRIS-NG validation ($n = 23$ spectra, 15 Delta-X stations plus 8 additional spectra from

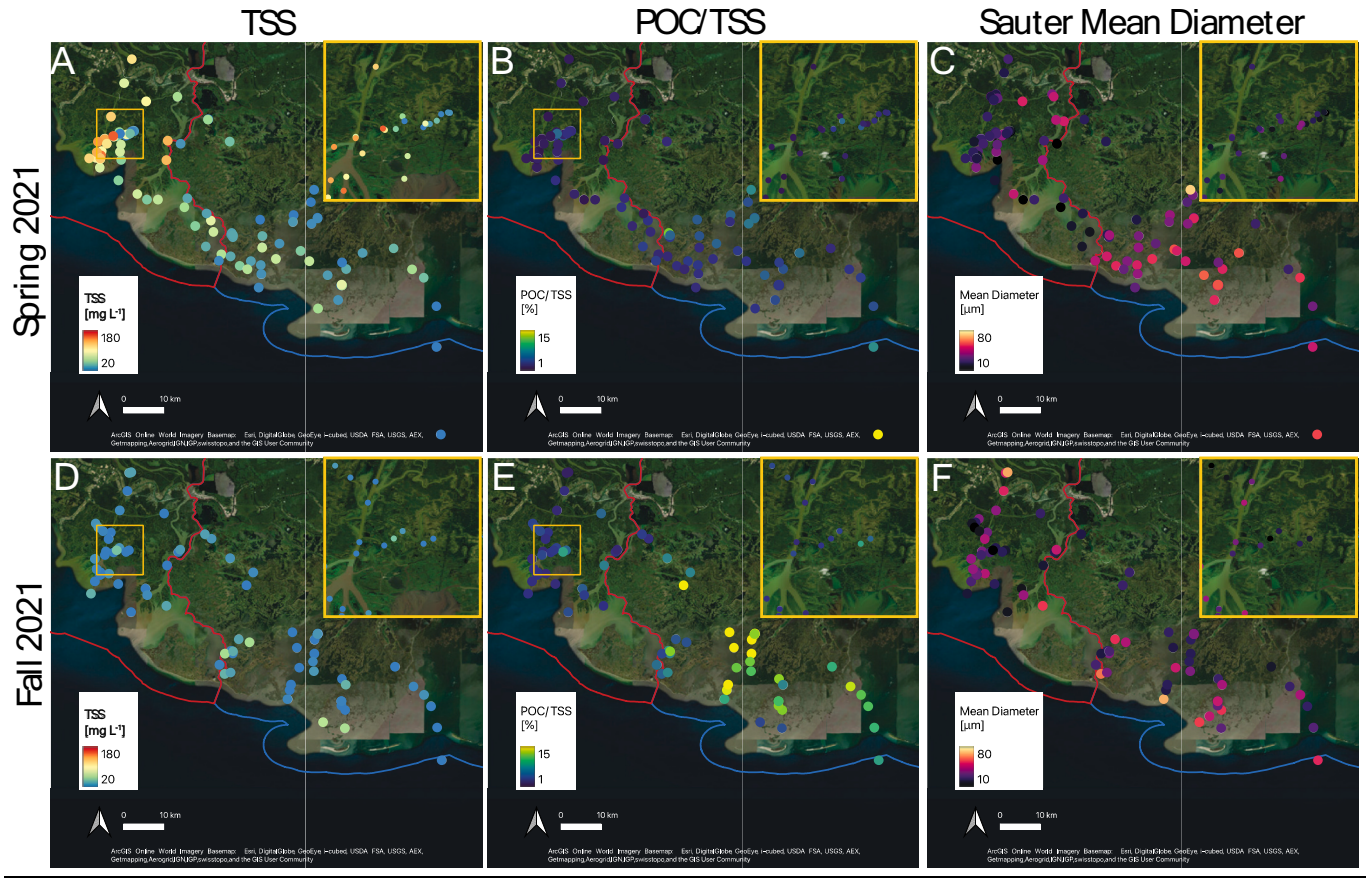

Fig. 2. Particle properties mapped from Delta-X in situ sampling. Particle properties including (A and D) TSS, (B and E) POC/TSS, and (C and F) Sauter Mean Diameter were measured across both basins during the spring and fall 2021 field campaigns to characterize spatial and seasonal variability of TSS concentration, particle composition, and size.

stations with multiple overpasses) included only the stations from the Delta-X campaign. Some stations were covered by multiple AVIRIS-NG images from the same day, which were used as multiple validation data points. Only the 15 Delta-X-derived matchup stations were used for validation of the POC/TSS algorithm.

2.7. HydroLight radiative transfer simulations

HydroLight radiative transfer simulations (Mobley et al., 2022) were run to model the R_{rs} at field stations. Simulations were run for the Case 2 optical model, using field-measured IOPs as inputs, including: chlorophyll-a concentration, chlorophyll-a-specific absorption coefficient ($a^*_\phi(\lambda) = a_\phi(\lambda)\,[chl-a]^{-1}$), CDOM absorption coefficient ($a_g(\lambda)$), mass-specific (i.e., normalized by TSS) non-algal particle absorption and scattering coefficients ($a^*_{NAP}(\lambda) = a_{NAP}(\lambda)\,[TSS]^{-1}$ and $b^*_p(\lambda) = 0.01833^{-1} b_{bp}(\lambda)\,[TSS]^{-1}$, with 0.01833 derived from the Petzold average particle (Mobley et al., 1993)). HydroLight was used for two applications:

1. validate R_{rs} at field stations where both in situ and AVIRIS-NG R_{rs} were measured, using field-measured IOPs as inputs; and
2. assess the influence of shallow water and bottom reflectance on TSS retrieval. The *Vis-NIR PLSR* algorithm was applied to HydroLight-output R_{rs} spectra for each TSS/depth scenario from 5 to 300 mg L^{-1} TSS and 0.1–4 m depth.

To assess the possible influence of bottom reflectance on TSS retrieved by the *Vis–NIR PLSR* algorithm, we conducted a suite of radiative transfer simulations with HydroLight using variable TSS concentrations (5–300 mg L^{-1}) and water depths (0.1–0.6 m) above a dark-sediment bottom, expected to be most similar to the muddy sediments encountered in the study area. Simulations were run for the Case 2 optical model, using the average optical properties (phytoplankton absorption and scattering, CDOM absorption, and non-algal mass-specific absorption and scattering) measured during the Delta-X spring campaign.

2.8. Spectral downsampling analysis

The impact of R_{rs} spectral resolution on TSS and POC/TSS algorithm performance was assessed by downsampling R_{rs} to coarser spectral resolution. Spectra were converted to the coarser spectral resolution (5–60 nm bandwidth) using Super-Gaussian spectral response functions (Ford and Vodacek, 2020), with full-width half-max equal to the spectral sampling spacing. To minimize the influence of band position on validation, downsampled bands were shifted by increments of 5 nm until all band center positions had been tested, and the central wavelength repeated (i.e., for 15 nm band spacing, bands were tested with the shortest wavelength band center at 432 nm, 437 nm, and 442 nm). Log-log PLSR algorithms for POC/TSS and TSS were calibrated for each set of downsampled bands, and the number of latent variables was selected such that adding additional latent variables no longer decreased the leave-one-out cross-validation mean absolute error. Retrieval accuracy was also compared to multiple-linear-regression algorithms developed for Landsat 8 OLI- and Sentinel 2 MSI-equivalent bands to compare the performance of simple MLR algorithms against the more complex and higher spectral resolution PLSR approaches.

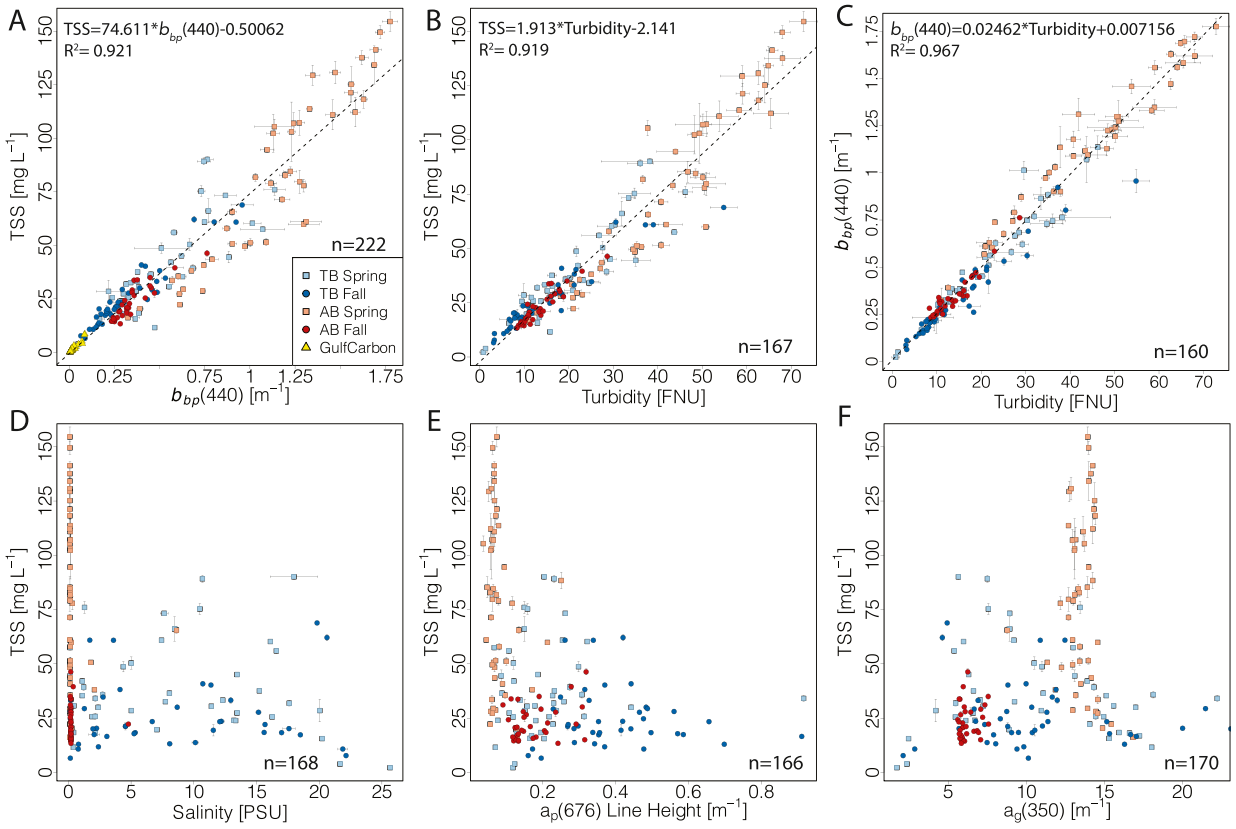

Fig. 3. Relationships between TSS concentration, particle backscattering coefficient, turbidity and other environmental parameters. (A) b_{bp} (440) vs. TSS, (B) Turbidity vs. TSS, and (C) Turbidity vs. b_{bp}(440) (D) Salinity vs. TSS, (E) particle absorption coefficient chlorophyll-a line height vs TSS, and (F) absorption coefficient of CDOM at 350 nm vs TSS. Slight differences in the number of stations where parameters were measured drove differences in the number of observations. Error bars represent one standard deviation measurement uncertainty. Dashed lines indicate the linear best-fit line.

3. Results and discussion

3.1. Concentration and Physico-chemical properties of suspended particles

Particle concentration and properties exhibited considerable spatial and seasonal variability. Across both basins, TSS concentrations were higher (Fig. 2A and D) and POC/TSS (Fig. 2B and E) was lower during the spring campaign than during the fall campaign. Seasonal differences in TSS concentration were particularly pronounced in the Atchafalaya Basin (spring median TSS: 79.7 mg L^{-1}; fall median TSS 20.8 mg L^{-1}). These TSS concentrations match historical values measured by the USGS in the Atchafalaya River (Welch et al., 2014). TSS in the Terrebonne basin, with less direct influence from Atchafalaya River discharge, was lower (spring median TSS: 32.6 mg L^{-1}; fall median TSS: 21.4 mg L^{-1}). TSS concentration was similar in both basins during the low discharge conditions of the fall, indicating a decrease in the influence of riverine waters on TSS concentration.

Waters influenced by high Atchafalaya River discharge during the spring campaign also had high mineral content (low POC/TSS). POC/TSS measured in the Atchafalaya Basin was similar in the spring and fall (spring median: 2.2% and fall median: 3.5%). These POC/TSS values matched previous measurement ranges of organic carbon fraction in suspended sediment (1.14–1.88%, Gordon and Goñi, 2003) and in sediment cores in the Atchafalaya Basin (approx. 0–2%, Bianchi et al., 2007; 0.56–2.87%, Gordon et al., 2001; 0–3.2%, Shields et al., 2019). Higher POC/TSS was measured in the Terrebonne Basin during the fall campaign (fall median: 11.1%) than in the spring (spring median: 4.0%). The highest POC/TSS values (> 20%) were measured in shelf waters beyond the barrier islands in the southern Terrebonne Basin and matched previously reported particulate carbon fraction measurements from the adjacent northern Gulf of Mexico (Epps, 2018; Trefry et al., 1994). At smaller spatial scales, TSS concentrations were lower and POC/TSS was higher in the low energy environments of small channels, such as the area shown in the inset panel of Fig. 2A, B, D, and E.

Trends in the spatio-temporal distribution of mean diameter were less clear. During the spring campaign (Fig. 2C), smaller particle diameters were encountered in the Atchafalaya Basin (spring median: 26.4 μm) than in the Terrebonne Basin (spring median: 41.0 μm). The fall campaign (Fig. 2F) lacked this spatial pattern (Atchafalaya median 35.4 μm, Terrebonne median 29.6 μm). Diameters occurred over a similar range to surface particle diameters measured during 2011 flooding (Kolker et al., 2014) at the mouth of the Atchafalaya River (< 50 μm) and were smaller than surface water particle diameters measured farther out on the shelf (~200 μm).

3.2. Inherent optical properties of suspended particles

3.2.1. Relationships with particle concentration

TSS concentration (0.09–154.5 mg L^{-1}, Fig. 3A and B) was linearly correlated ($R^2 = 0.921$ for b_{bp}(440) and $R^2 = 0.919$ for turbidity) with its two optical proxies (Doxaran et al., 2016; Neukermans et al., 2012b). b_{bp}(440) and turbidity were even more correlated ($R^2 = 0.967$, Fig. 3C). These relationships exhibited some variability resulting in deviations from the fitted lines. In the spring campaign, b_{bp} per TSS was higher in the Atchafalaya Basin than in Terrebonne at moderate TSS concentration (25–75 mg L^{-1}). At the highest TSS concentrations (> 100 mg L^{-1})—observed only during the spring campaign in the Atchafalaya Basin—mass-specific b_{bp} (TSS-normalized), b^*_{bp}, was lower than for other Atchafalaya Basin stations. In the fall campaign, b^*_{bp} was higher in the

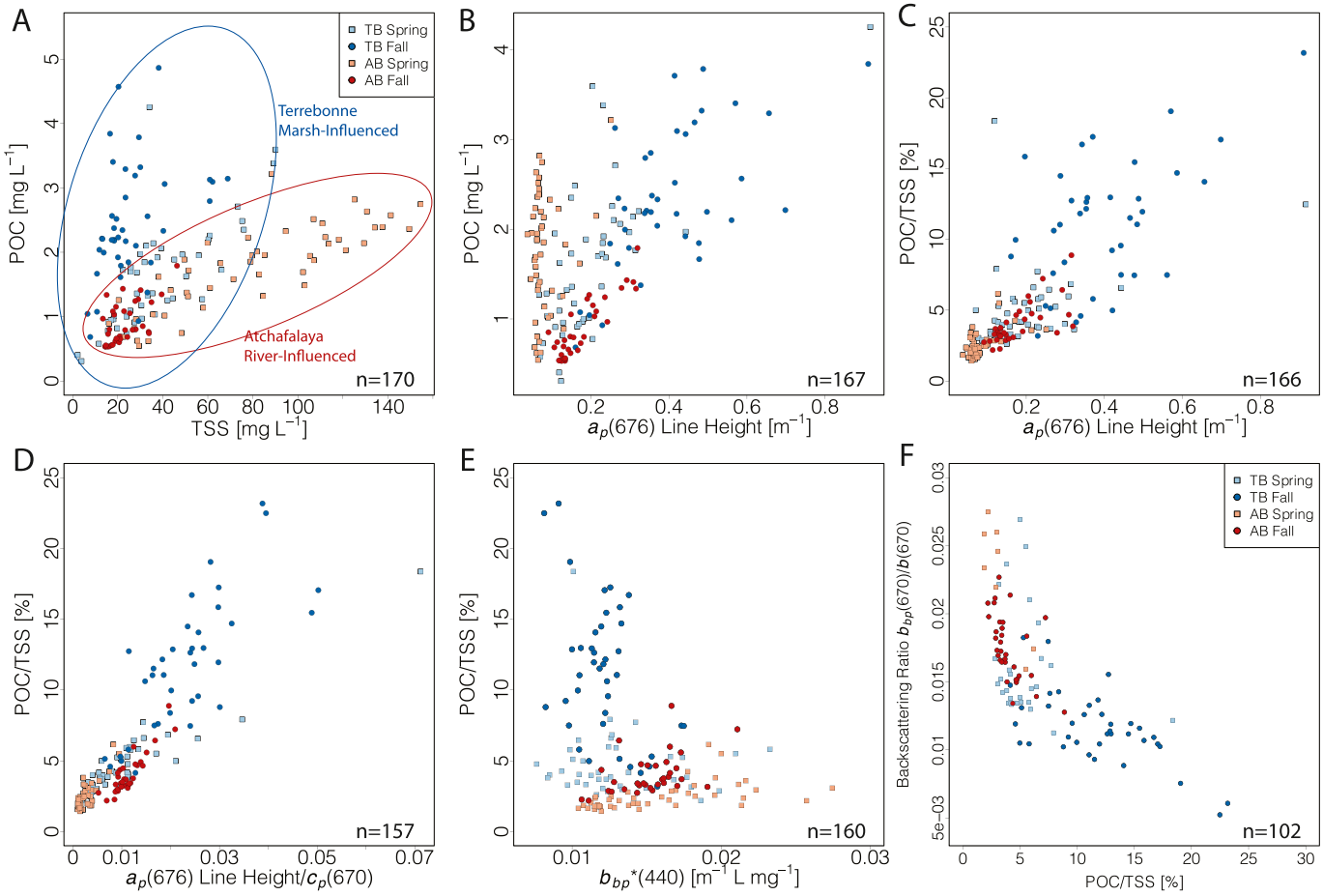

Fig. 4. In situ POC related to TSS and particle inherent optical properties. (A) TSS vs POC exhibited different relationships between the two basins, indicating that POC/TSS is a measure of varying particle composition. An optical chlorophyll-a proxy (B) a_p(676) line height only partially explained variability in POC and was better-correlated with (C) TSS-normalized carbon content POC/TSS, particularly (D) when a_p(676) was normalized by a proxy for total particles c_p(670). POC/TSS was also associated with differences in (E) the mass-specific backscattering coefficient and (F) backscattering ratio of suspended particles.

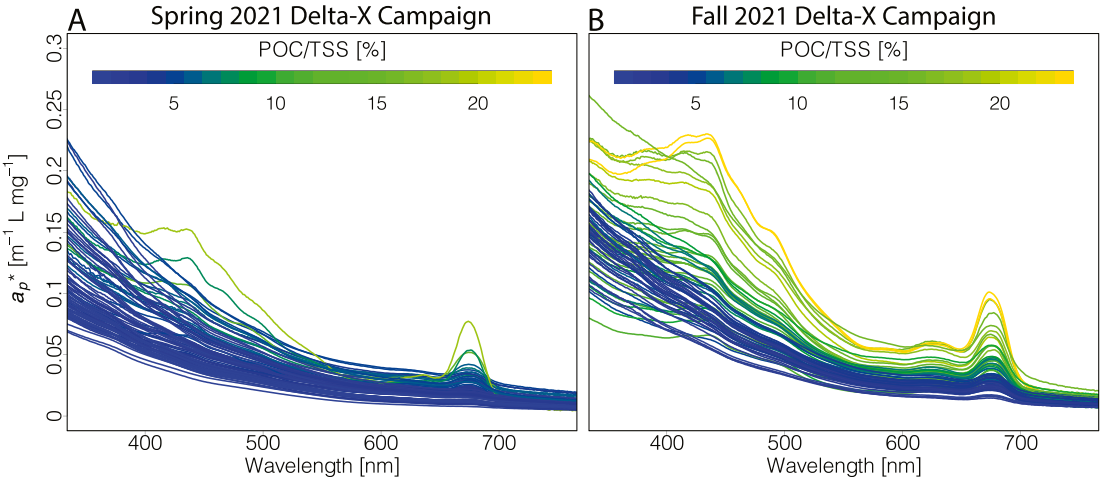

Fig. 5. Mass-specific (TSS-normalized) particulate absorption coefficient, a_p^*, spectra colored by POC/TSS from (A) Spring 2021 Delta-X Campaign, (B) Fall 2021 Delta-X Campaign.

Atchafalaya Basin than in the Terrebonne Basin across all TSS concentrations (6.58–68.9 mg L^{-1}).

Variability in b_{bp}^* has previously been associated with differences in the composition and size distribution of suspended particles (Neukermans et al., 2012a; Slade and Boss, 2015). The seasonally variable contribution of river discharge, which carries mineral-rich (low POC/TSS) particles (Bianchi et al., 2011; Schartau et al., 2019; Shields et al., 2019), is a primary control on particle properties in this system. Increased phytoplankton concentration (Schartau et al., 2019) during the fall campaign may have increased POC/TSS, particularly in the

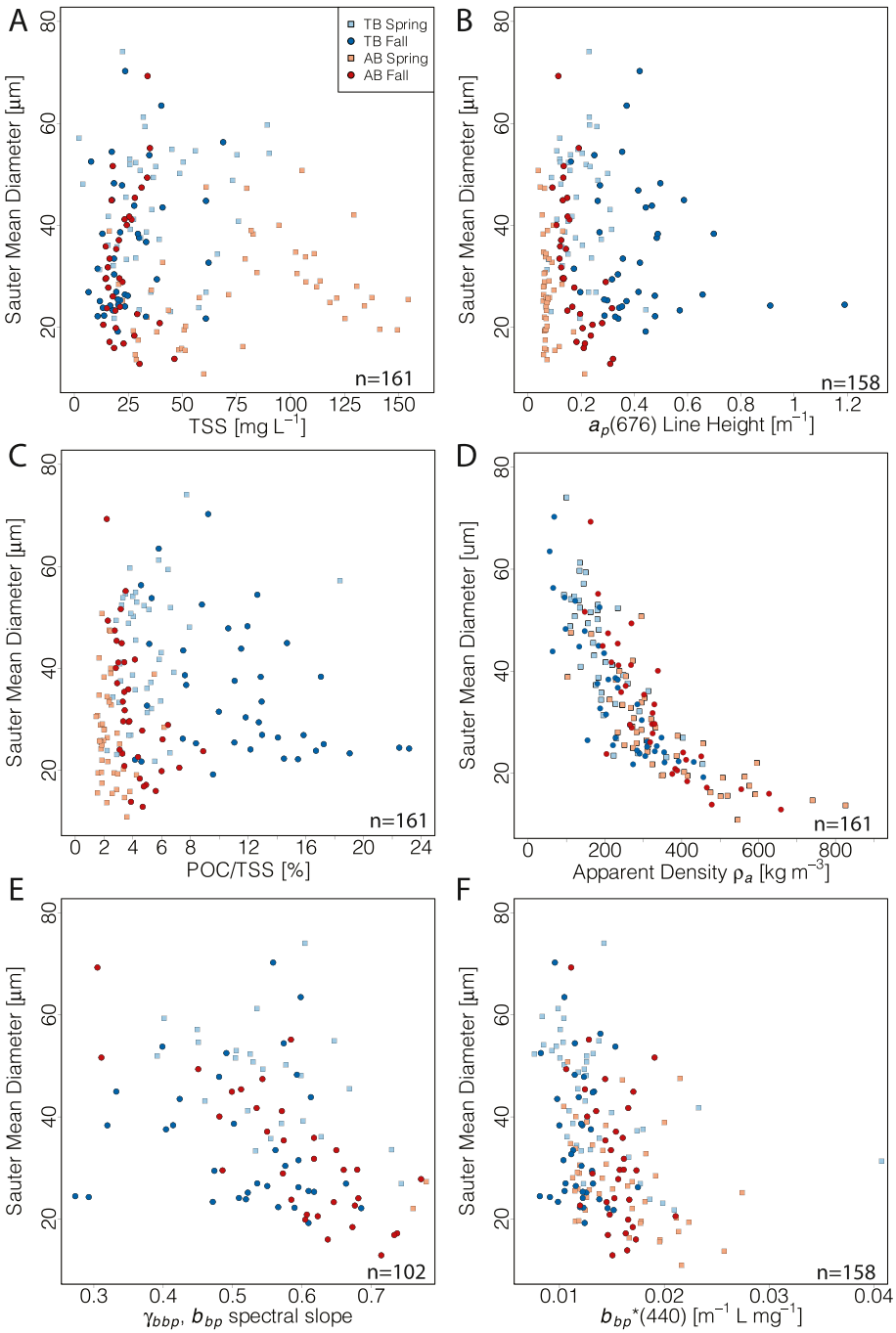

Fig. 6. Relationship between particle Sauter mean diameter and other environmental and optical conditions. Mean diameter was not well-correlated with (A) TSS, (B) a_p(676) line height, or (C) POC/TSS. There was a clear non-linear relationship (D) between decreasing Sauter mean diameter and particle apparent density. Backscattering properties have been found to correlate well with mean particle diameter in previous studies to backscattering properties including (E) backscattering spectral slope $\gamma_{b_{bp}}$ and (F) b_{bp}*(440). There was not a clear relationship between particle size and backscattering properties in the Delta-X field data.

Terrebonne Basin where phytoplankton productivity can be high during the summer months (Sweet et al., 2022). TSS concentration varied independently from salinity, a_p line height (the size of a peak in a_p at 676 nm, used as a proxy for chlorophyll-a concentration (Roesler and Barnard, 2013)), or a_g(350) (Fig. 3D–F), a proxy for dissolved organic matter content.

3.2.2. *Relationships with particle composition*

In situ POC concentration exhibited multiple, distinct relationships with TSS and other parameters, indicative of differences in particle type (Fig. 4A). In situ POC occurred at higher concentrations than had been previously measured farther out on the continental shelf (Le et al., 2017), although high nearshore POC is compatible with the previously observed pattern of increasing POC closer to shore. The Atchafalaya Basin samples during the spring campaign (pink squares, Fig. 4B and C) exhibited relatively high POC but low POC/TSS and a_p line height, suggesting the high POC is largely detrital and driven by the high TSS concentration from the river. High POC/TSS and the strong relationship between chlorophyll-a and POC/TSS in the Terrebonne Basin indicate that POC in Terrebonne basin is largely driven by phytoplankton biomass, matching previous observations (Sweet et al., 2022). POC/TSS was strongly correlated (Fig. 4C and D) with a_p line height and a_p line

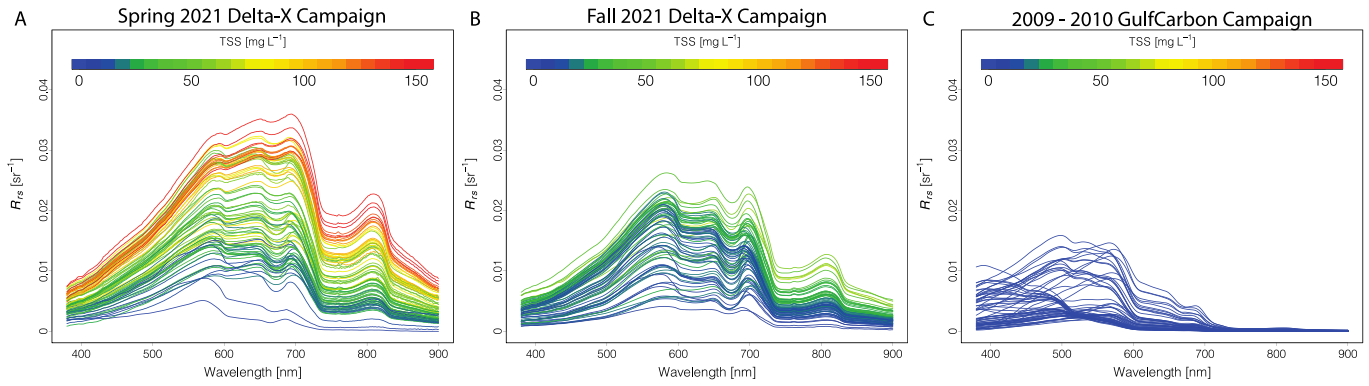

Fig. 7. Remote sensing reflectance (*Rrs*) spectra measured during the field campaigns compared to TSS concentration. R_{rs} spectra colored by TSS from (A) Spring 2021 Delta-X Campaign, (B) Fall 2021 Delta-X Campaign, and (C) 2009–2010 GulfCarbon campaign.

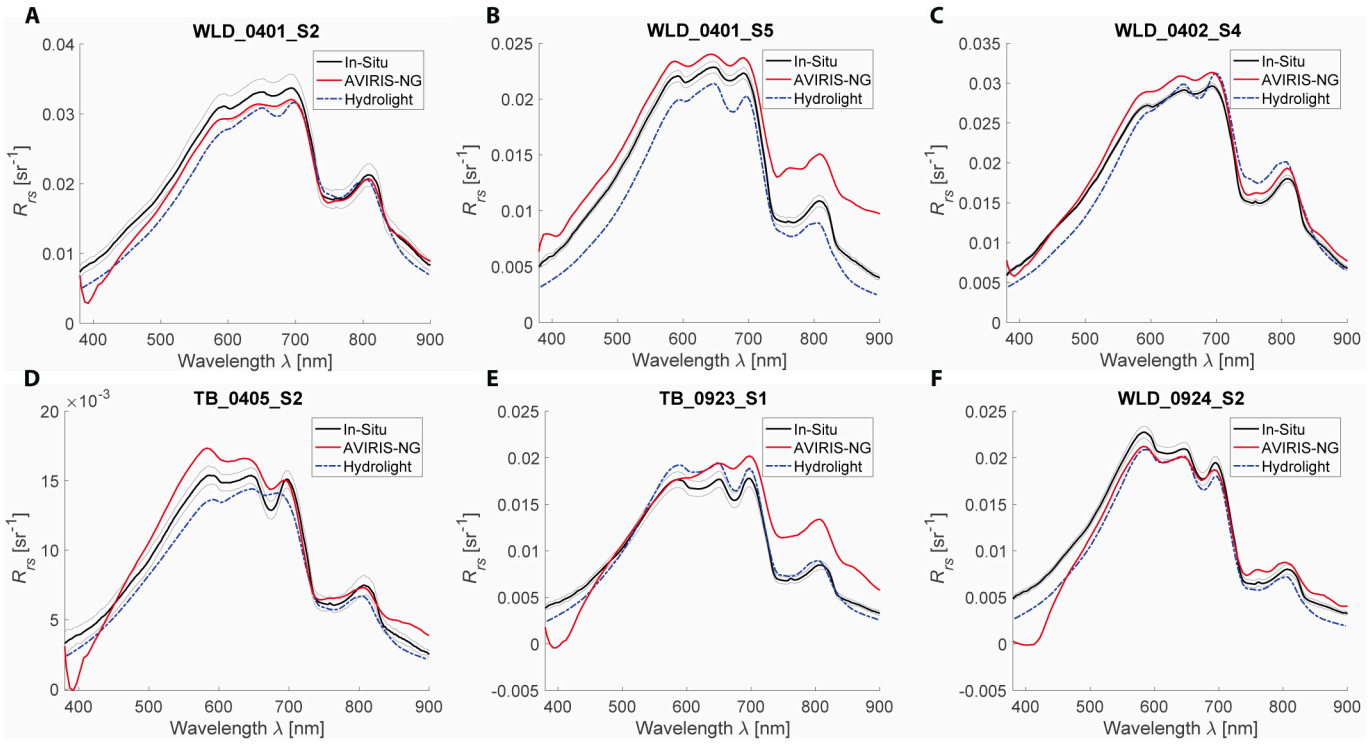

Fig. 8. *Rrs* from a representative subset of stations where in situ and concurrent/collocated AVIRIS-NG *Rrs* spectra were collected. *Rrs* spectra derived from HydroLight simulations, informed by field measurements of water IOPs, are presented for comparison. *Rrs* spectra from all 15 validation stations with high-quality in situ and AVIRIS-NG R_{rs} are presented in Supplementary Fig. S4. In-situ R_{rs} measurement uncertainty (1 standard deviation) is represented as a gray-shaded area.

height/$c_p(670)$, a proxy for phytoplankton biomass normalized to a proxy for TSS concentration. Previous research (e.g., Bowers et al., 2014) has identified the influence of POC/TSS on particle scattering properties. POC/TSS showed non-linear relationships with particle backscattering properties including $b^*_{bp}(440)$ (Fig. 4E) and the ratio of backscattering to total particulate scattering $b_{bp}(670)/\ b_p(670)$ (Fig. 4F).

POC/TSS also acted as a strong control on the mass-specific absorption coefficient (a^*_p, a_p normalized by TSS) of suspended particles (Fig. 5). Samples that were higher in POC/TSS had increased a^*_p at all wavelengths and pigment absorption peaks in the a^*_p spectrum near 676 nm and 440 nm. POC/TSS had a strong influence on particle IOPs, suggesting likely avenues for retrieving carbon content from R_{rs}.

3.2.3. *Relationships with particle size*

No strong relationship was observed in the Delta-X dataset between particle Sauter mean diameter and TSS, $a_p(676)$ line height, POC/TSS (Fig. 6A–C), or R_{rs}. Mean diameter appeared correlated with TSS in stations from the Atchafalaya Basin with the highest TSS, but this relationship did not extend to other field sampling stations even from the same basin and season. As noted in other studies of flocculated particles (Khelifa and Hill, 2006), Sauter mean diameter decreased non-linearly with particle apparent density (Fig. 6D). Apparent density was not a simple function of POC/TSS and was likely also influenced by the packing geometry of particle aggregates. Previous studies (Slade and Boss, 2015; Stramski et al., 2007) identified relationships between particle mean diameter and backscattering spectral slope $\gamma_{b_{bp}}$ and mass-specific backscattering b_{bp}*(440). Here, particle diameter varied only weakly with these backscattering properties (Fig. 6E and F). Overall, these weak relationships between particle size and inherent optical properties prevented the development of a robust optical proxy. Particle scattering slope and particle size have been previously retrieved in the Atchafalaya Basin (Shi and Wang, 2019), albeit without in situ

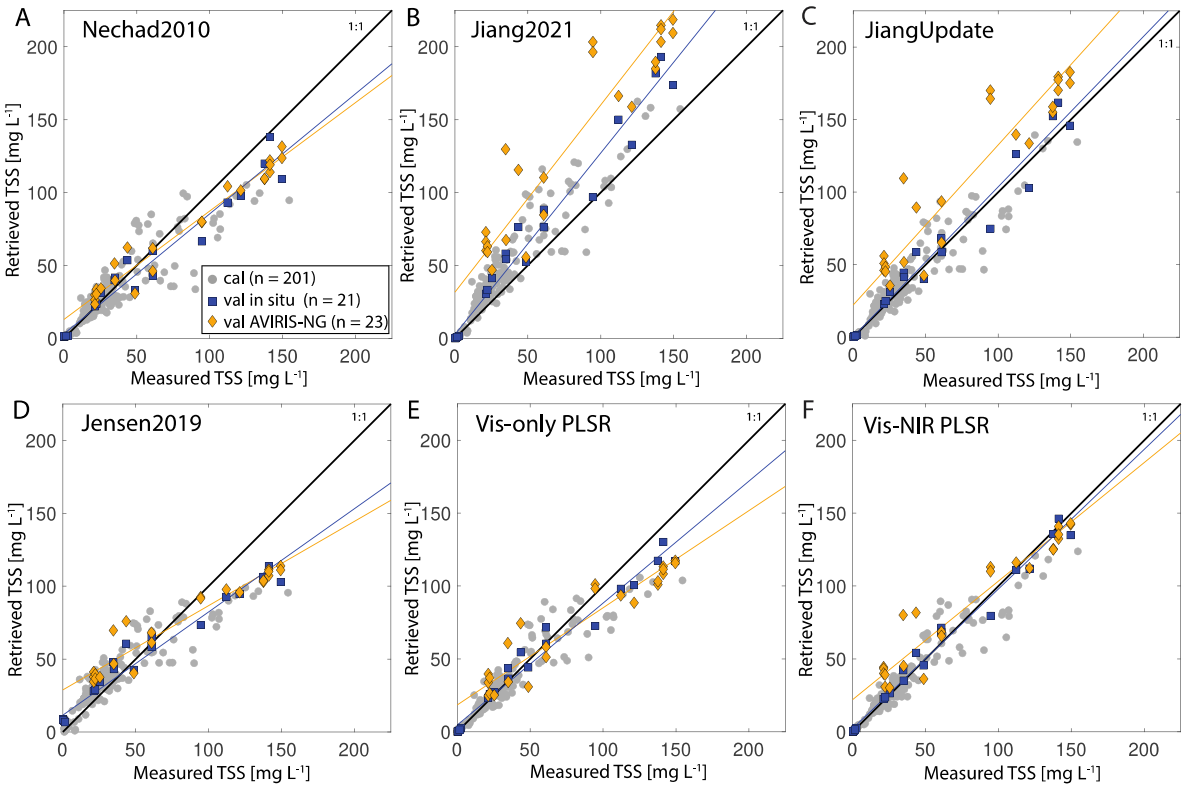

Fig. 9. TSS algorithm performance using in situ R_{rs} for calibration (gray circles) and in situ validation (blue squares) and using collocated/simultaneous AVIRIS-NG R_{rs} for validation (orange diamonds). Reference algorithms were tested: (A) *Nechad2010*, (B) *Jiang2021*, (C) *JiangUpdate*, and (D) *Jensen2019*. Two new empirical algorithms were also tested: (E) *Vis-Only PLSR* and (F) *Vis–NIR PLSR*. (For interpretation of the references to colour in this figure legend, the reader is referred to the web version of this article.)

Table 3
Error summary statistics of in situ and AVIRIS-NG TSS algorithm validation.

Algorithm	R^2 In Situ	R^2 AVIRIS	MAPD In Situ [%]	MAPD AVIRIS [%]	Median Bias In Situ [mg L^{-1}]	Median Bias AVIRIS [mg L^{-1}]	Slope In Situ	Slope AVIRIS
Nechad2010	0.98	**0.98**	23.1	19.3	**0.091**	−14.6	0.823	0.744
Jiang2021	**0.99**	0.93	36.7	81.3	11.5	51.7	1.25	1.28
JiangUpdate	0.98	0.93	17.9	40.0	**−0.011**	27.4	**1.04**	**1.11**
Jensen2019	0.98	0.96	31.4	24.6	5.13	**−2.04**	0.708	0.578
Vis-Only PLSR	**0.99**	0.95	12.5	21.5	**−0.098**	**−2.64**	0.836	0.667
Vis–NIR PLSR	**0.99**	0.95	**6.67**	**16.3**	**0.132**	6.71	**0.958**	0.813

Table 4
Error summary statistics of in situ and AVIRIS-NG POC/TSS algorithm validation.

Algorithm	R^2 In Situ	R^2 AVIRIS	MAPD In Situ [%]	MAPD AVIRIS [%]	Median Bias In Situ [%]	Median Bias AVIRIS [%]	Slope In Situ	Slope AVIRIS
POC/TSS Vis–NIR PLSR	0.96	0.89	7.31	7.60	−0.034	0.008	0.952	0.903

validation. We attempted to retrieve of b_{bp} spectral slope and Sauter mean diameter from R_{rs} using log-log PLSR, but this approach was unsuccessful.

3.3. Water remote sensing reflectances

Higher TSS was associated with increased red and NIR R_{rs}, which reached values >0.035 sr^{-1}, in the Delta-X and GulfCarbon campaigns (Fig. 7). The shape of the R_{rs} spectra also varied between seasons. Reflectance spectra from the spring campaign often peaked in the red or green range. In contrast, reflectance often peaked in the green in spectra from the fall campaign, and in the blue in spectra from the GulfCarbon campaigns. Differences in spectral shape were caused by independent variability in the amount of CDOM, phytoplankton, and detrital particles (Mouw et al., 2015; Sathyendranath, 2000). The differences in a_p^* shown in Fig. 5 are also expected to contribute to the different R_{rs} spectral shapes between campaigns. Differences in spectral shape of R_{rs} are particularly visible at the location of pigment absorption peaks (440 nm and 676 nm) identified in the a_p^* spectra.

Good agreement was observed between collocated, near-simultaneous in situ, HydroLight, and AVIRIS-NG R_{rs} from the 15 Delta-X-derived validation stations (Fig. 8, Supplementary Fig. S4). In

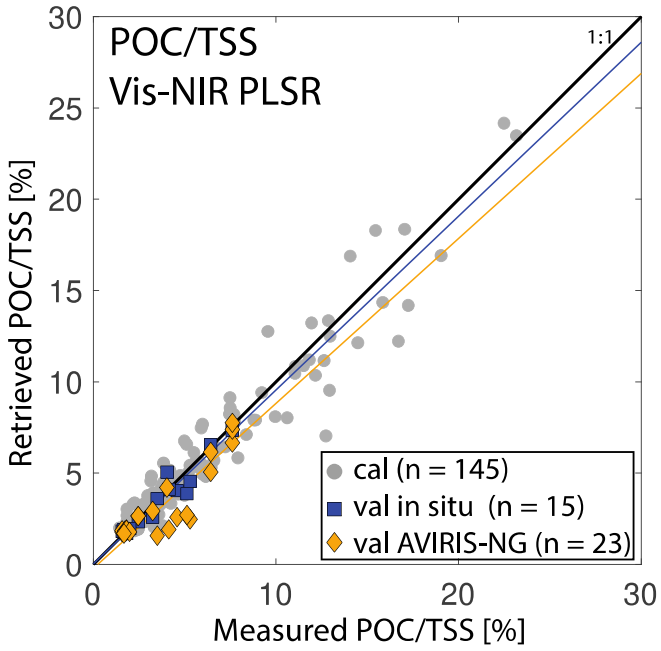

Fig. 10. *POC/TSS PLSR* algorithm performance using in situ R_{rs} for calibration (gray circles) and in situ validation (blue squares) and using collocated/simultaneous AVIRIS-NG R_{rs} for validation (orange diamonds). POC/TSS PLSR algorithm utilized 7 latent variables. (For interpretation of the references to colour in this figure legend, the reader is referred to the web version of this article.)

situ and HydroLight-modeled R_{rs} spectra were very similar in both shape and magnitude, providing confidence in the quality of the in situ R_{rs}. At some stations, in situ and HydroLight R_{rs} differed slightly, possibly due to minor spatial and temporal mismatch between radiometry and HydroLight input IOP measurements, or due to limitations in the HydroLight parameterization or solver, or in situ reflectance uncertainties. The AVIRIS-NG R_{rs} spectra also matched in situ R_{rs} well (e.g., Fig. 8A and C), but spectra at some stations had substantial mismatch. Two main types of mismatches were observed: low AVIRIS-NG R_{rs} in the UV–blue (380–450 nm) range (Fig. 8D–F) and high AVIRIS-NG R_{rs} in the red–NIR (730–900 nm) range (Fig. 8B and E).

Low AVIRIS-NG R_{rs} in the UV–blue range was more common during the fall Delta-X campaign, when atmospheric humidity was high, and could be related to uncertainty in atmospheric aerosols (Frouin et al., 2019). Drift in detector gain coefficients between the two campaigns is another possibility. Errors in UV–blue R_{rs} likely had minimal impacts on TSS and POC/TSS retrieval, as algorithms primarily used longer wavelengths. High AVIRIS-NG R_{rs} in the red–NIR range appeared related to scattered light from adjacent land pixels (Bulgarelli and Zibordi, 2018)—notably healthy terrestrial vegetation is highly reflective in the NIR. AVIRIS-NG R_{rs} spectra with this type of mismatch differed in shape from the near-universal red–NIR spectral shape for aquatic targets (Ruddick et al., 2006). Spuriously high AVIRIS-NG red–NIR R_{rs} may have caused overestimation of TSS near land-water boundaries. These adjacency effects are discussed in greater detail in Appendix A5.

3.4. TSS algorithm validation

TSS algorithm accuracy was assessed using summary statistics from in situ and AVIRIS-NG-derived validation. Algorithms were assessed using model-II regression R^2, median absolute percent difference (MAPD), median bias, and model-II regression slope between measured and retrieved values.

3.4.1. In situ TSS algorithm validation

The *Vis–NIR PLSR* algorithm retrieved TSS with the highest accuracy and minimal bias during in situ calibration and validation ($R^2 = 0.99$, MAPD = 6.67%, bias = 0.132 mg L^{-1}, and slope = 0.958). *Vis–NIR PLSR* outperformed the other algorithms by accurately retrieving TSS at both high (> 100 mg L^{-1}) and low (< 10 mg L^{-1}) TSS concentrations (Fig. 9 and Table 3). In comparison, the *Nechad2010* (Fig. 9A, slope = 0.823) and *Jensen2019* (Fig. 9D, slope = 0.708) algorithms both underpredicted TSS at higher concentrations, likely due to using few high-TSS samples for calibration. The *Jiang2021* algorithm (Fig. 9B) overestimated TSS at all concentrations (bias = 11.5 mg L^{-1}). The *JiangUpdate* (Fig. 9C), which updated only the conversion of retrieved b_{bp} to TSS, did not overestimate TSS during in situ validation. However, the *JiangUpdate* still had higher MAPD and bias (MAPD = 17.9%) than the *Vis–NIR PLSR*.

The *Vis-Only PLSR* algorithm (Fig. 9E) performed well at low and moderate TSS concentrations, but underpredicted TSS at concentrations greater than ~100 mg L^{-1} (slope = 0.836). Other studies (Dogliotti et al., 2015; Jiang et al., 2021) have identified the saturation of red reflectance as a limitation of visible-only TSS retrieval and described the advantages of NIR R_{rs} in turbid waters. Red reflectance saturation may have also impacted *Nechad2010* at high TSS concentrations, as it used R_{rs}(712.5).

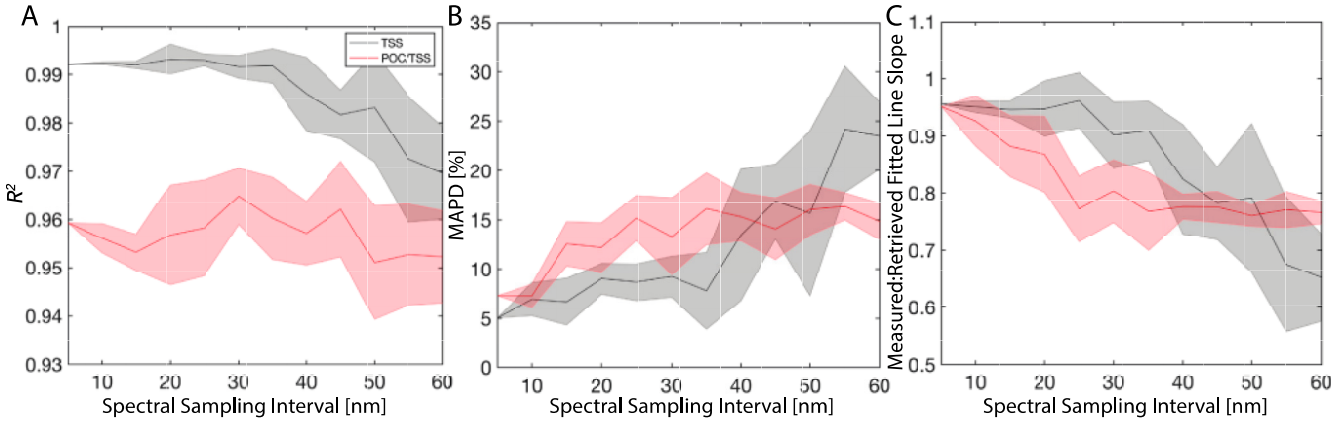

Fig. 11. Effect of spectral resolution on TSS (gray) and POC/TSS (red) retrieval accuracy. Accuracy of in situ validation was tested for log-log PLSR algorithms applied to R_{rs} spectra downsampled from AVIRIS-NG native 5 nm spectral sampling to 60 nm spectral sampling. Validation accuracy was assessed using (A) R^2, (B) MAPD, and (C) slope of the model-II best fit line through measured versus retrieved parameters. (For interpretation of the references to colour in this figure legend, the reader is referred to the web version of this article.)

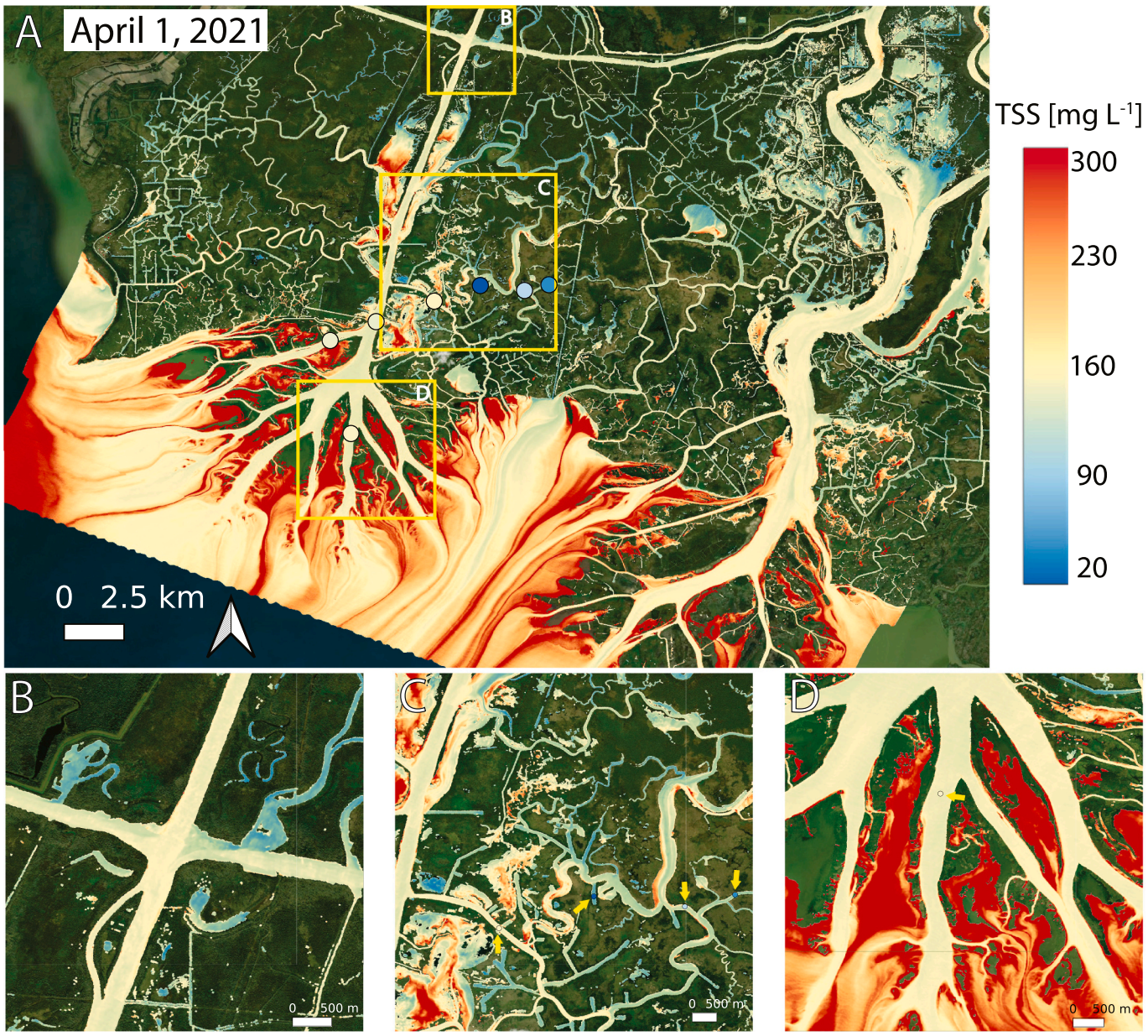

Fig. 12. TSS retrieval over the Atchafalaya Basin on April 1, 2021 (In situ TSS 20.4–154.5 mg L^{-1}) at high seasonal river discharge. TSS was mapped (A) over the entire basin. Insets show higher resolution images of (B) the intersection of the intracoastal waterway and the Wax Lake Outlet, (C) secondary channels extending into forested freshwater marshes, and (D) the Wax Lake Delta focusing on central islands. Points indicate the location of field sampling stations collected on April 1, 2021, and are displayed on the same color scale as the imagery (field sampling stations are highlighted with yellow arrows). (For interpretation of the references to colour in this figure legend, the reader is referred to the web version of this article.)

3.4.2. *AVIRIS-NG TSS algorithm validation*

TSS retrieval was less accurate when validated using AVIRIS-NG-derived R_{rs} than from the corresponding in situ R_{rs}. The *Vis–NIR PLSR* algorithm (Fig. 9F) retrieved TSS most accurately in the end-to-end AVIRIS-NG validation (R^2 = 0.95, MAPD = 16.3%, Bias = 6.71 mg L^{-1}, and slope = 0.813). *Nechad2010* (Fig. 9A) performed relatively well, with better validation R^2 than *Vis–NIR PLSR*. However, the *Nechad2010* (Fig. 9A, slope = 0.744), *Jensen2019* (Fig. 9D, slope = 0.578) and *Vis-Only PLSR* (Fig. 9E, slope = 0.667) algorithms underestimated TSS at high sediment concentrations, as in the in situ validation. The *Jiang2021* algorithm (Fig. 9B, bias = 51.7 mg L^{-1}) and the *JiangUpdate* algorithm (Fig. 9C, bias = 27.4 mg L^{-1}) both overestimated TSS during AVIRIS-NG validation, though the *JiangUpdate* had the best slope (slope = 1.11). Adjacency effects in the NIR (Bulgarelli and Zibordi, 2018; Martinez-Vicente et al., 2013) may have substantially affected AVIRIS-NG validation accuracy (adjacency discussed in Appendix A5) for the Jiang algorithms as they rely exclusively on far-red and NIR wavelengths in turbid waters. A sensitivity to uncertainty in NIR atmospheric correction could also be a reason to use the *Vis-Only PLSR* over the *Vis–NIR PLSR* despite the better performance of the *Vis–NIR PLSR* in the absence of atmospheric uncertainties. A comparison of map artifacts created by the different algorithms is presented in Appendix A6.

3.5. *POC/TSS algorithm validation*

Retrieval of POC/TSS was validated using in situ and AVIRIS-NG spectra from 15 validation stations collected during the Delta-X campaign. The PLS-regression-based algorithm retrieved POC/TSS (Table 4 and Fig. 10) with a high degree of accuracy during in situ validation (R^2 = 0.96, MAPD = 7.31%, Bias = −0.034 mg L^{-1}, and slope

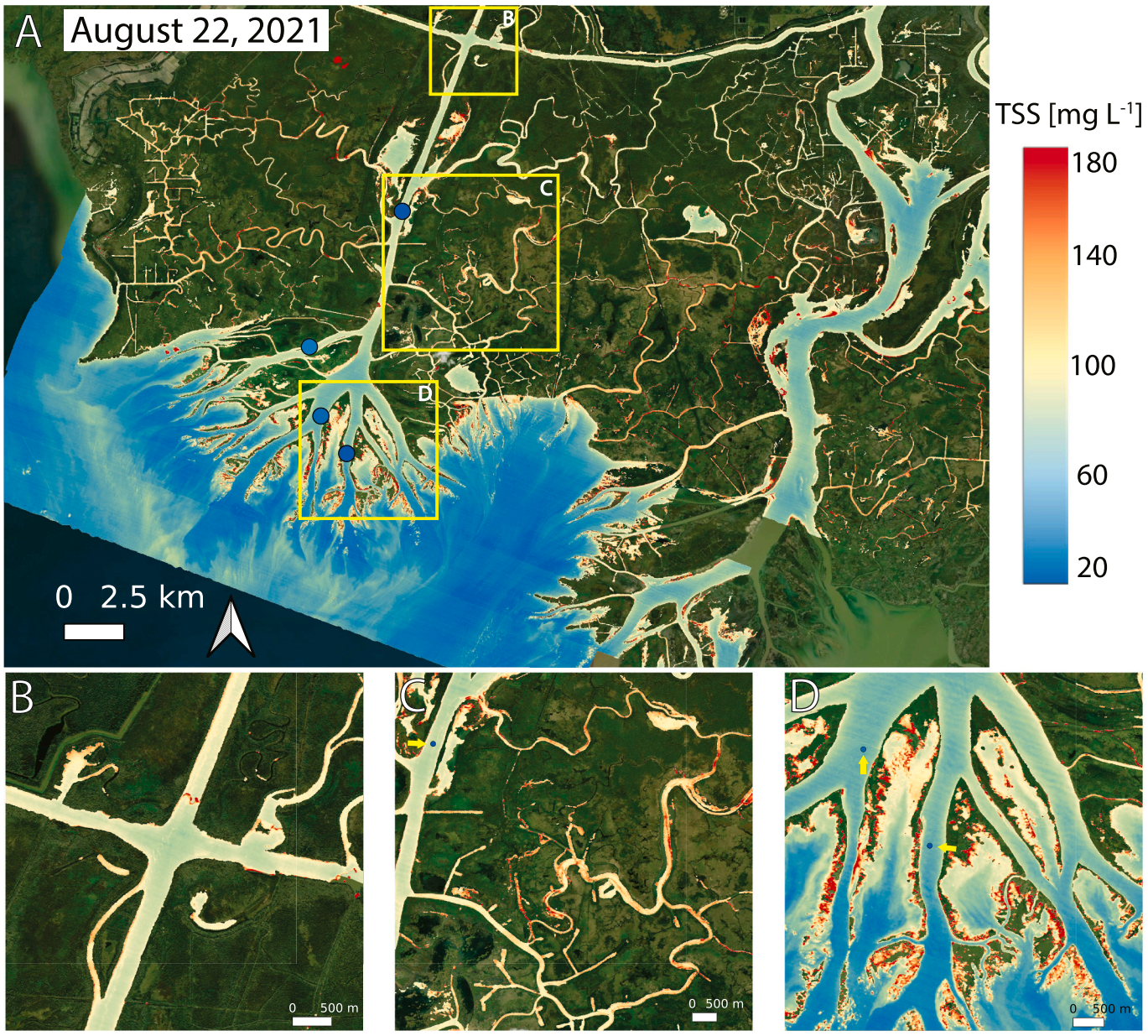

Fig. 13. TSS retrieval over the Atchafalaya Basin on August 22, 2021 (in situ TSS 19.4–33.9 mg L^{-1}) at low seasonal river discharge. TSS was mapped (A) over the entire basin. Insets show higher resolution images of (B) the intersection of the intracoastal waterway and the Wax Lake Outlet, (C) secondary channels extending into forested freshwater marshes, and (D) the Wax Lake Delta focusing on central islands. Points indicate the location of field sampling stations collected on August 22, 2021, and are displayed on the same color scale as the imagery (field sampling stations are highlighted with yellow arrows). (For interpretation of the references to colour in this figure legend, the reader is referred to the web version of this article.)

= 0.952). Validation using AVIRIS-NG-derived spectra retrieved POC/TSS accurately (R^2 = 0.89, MAPD = 7.6%, Bias = 0.008 mg L^{-1}, and slope = 0.903), but slightly less accurately than during in situ POC/TSS validation. POC/TSS retrieval may have been particularly sensitive to uncertainty in the AVIRIS-NG-derived R_{rs} spectra, because the influence of POC/TSS on R_{rs} is subtler than for TSS: similar R_{rs} uncertainty could contribute to greater uncertainty in POC/TSS than in TSS retrieval.

3.6. Spectral resolution and calibration data needs

This study demonstrated that utilizing NIR reflectance in the *Vis-NIR PLS* provided performance advantages at higher TSS concentrations (> 100 mg L^{-1}), where the otherwise similar *Vis-Only PLSR* underestimated TSS. This is consistent with existing studies indicating that NIR reflectance facilitates TSS retrieval at high concentrations (Dogliotti et al., 2015; Jiang et al., 2021). Use of NIR R_{rs} can however present additional uncertainty, as variability in aerosol concentration and characteristics can increase atmospheric correction uncertainty in nearshore and inland waters (Renosh et al., 2020; Thompson et al., 2019), and adjacency effects in these areas can present additional challenges in the NIR range. These uncertainties were magnified in challenging atmospheric conditions of the Delta-X Fall Campaign.

A direct assessment of TSS and POC/TSS retrieval over varying spectral resolutions (downsampled from 5 nm spectral sampling to 60 nm spectral sampling) indicated that POC/TSS retrieval accuracy was more sensitive to spectral resolution than TSS retrieval (Fig. 11). TSS retrieval improved (increased R^2, decreased MAPD, and increased slope) with decreasing spectral sampling interval when the spectral sampling interval was >20 nm, but had only small improvements once spectral sampling interval was ≤ 20 nm. POC/TSS retrieval improved with

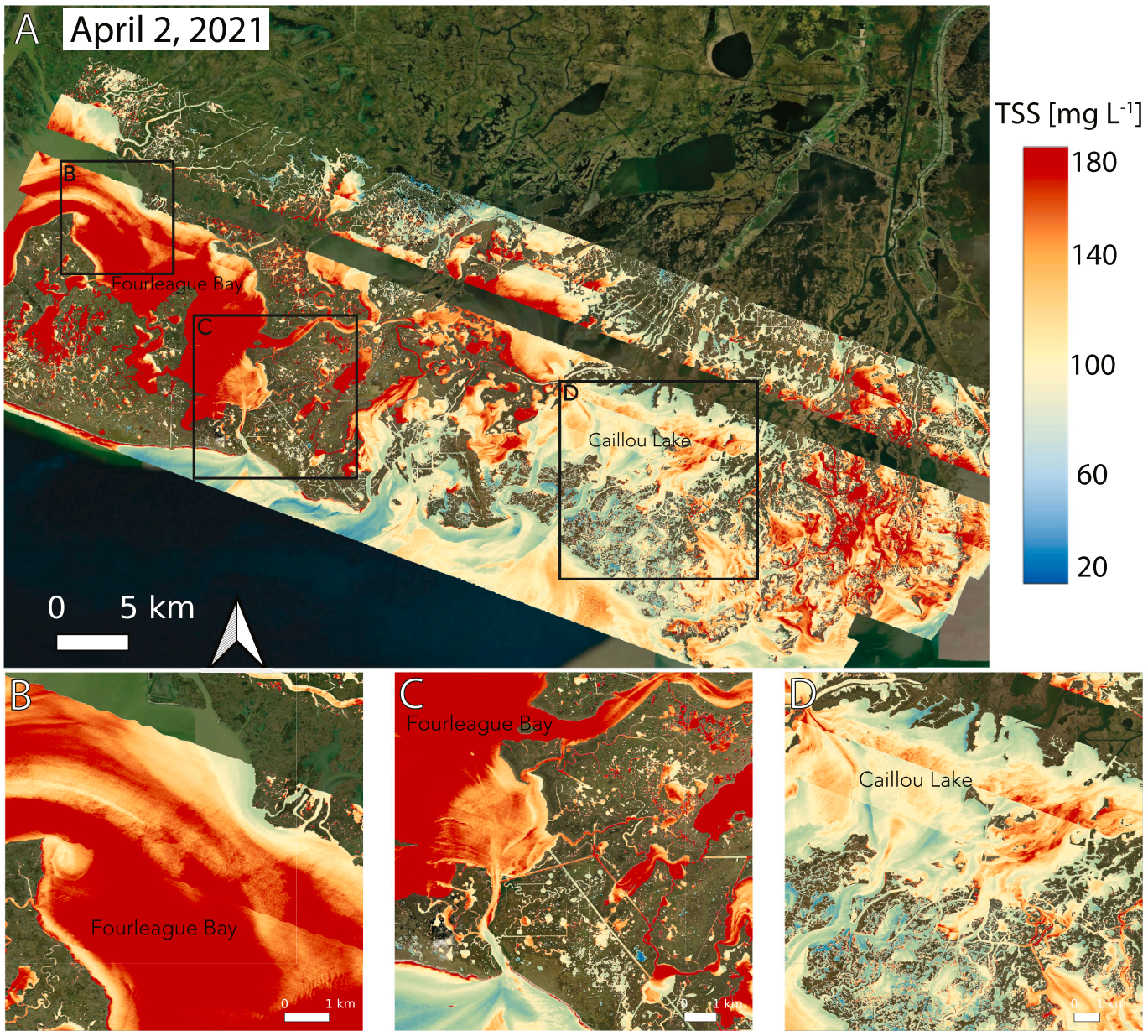

Fig. 14. TSS retrieval over the Terrebonne Basin on April 2, 2021, at high seasonal river discharge. TSS was mapped (A) over the entire basin. Insets show (B) northwestern Fourleague Bay, which receives sediment from the Atchafalaya River during high discharge; (C) southeastern Fourleague Bay, which connects to the continental shelf; and (D) Caillou Lake a shallow area mostly insulated from riverine inputs and primarily influenced by wind and tides.

decreasing spectral sampling over all spectral sampling intervals, with the greatest improvement as sampling interval went from 20 nm to 5 nm. The advantages of high spectral resolution R_{rs} was also demonstrated by comparing the *Vis-NIR PLSR* algorithm performance to multiple-linear-regression algorithms, tested on Landsat 8 OLI and Sentinel 2 MSI equivalent bands (Appendix A7). These MLR algorithms did not retrieve TSS as accurately as the PLSR-based approach, demonstrating the performance advantages of harnessing hyperspectral R_{rs} using PLSR for TSS retrieval.

High-quality calibration data that fully captures the range of variability is also essential for algorithm performance. This advantage is evident when comparing the *Jensen2019* algorithm to the structurally similar *Vis–NIR PLSR* and *Vis-Only PLSR* approaches: *Jensen2019* performed comparably well over TSS concentrations included in its calibration data (~20–70 mg L^{-1}) but retrieved TSS less accurately for concentrations outside this range. Though universally transferable algorithms might be preferable, the local, empirical *Vis–NIR PLSR* algorithm retrieved TSS more accurately over the full range of encountered conditions than the more broadly designed *Jiang2021* and *Nechad2010* algorithms. *Jiang2021* was also improved in the *JiangUpdate*, which replaced general particle optical properties with local values. Field measurements also facilitated algorithm validation, and the removal of images where high-altitude clouds negatively impacted the agreement between in situ and airborne R_{rs}.

3.7. Mapping particle concentration and properties with AVIRIS-NG

3.7.1. Seasonal trends and spatial features in TSS

TSS was mapped using a mosaic of AVIRIS-NG images collected on the same day to cover an entire basin. Four mosaics are presented (Thompson et al., 2023):

1. the Atchafalaya Basin on April 1, 2021, capturing high discharge and very high TSS in a river-influenced area (Fig. 12);

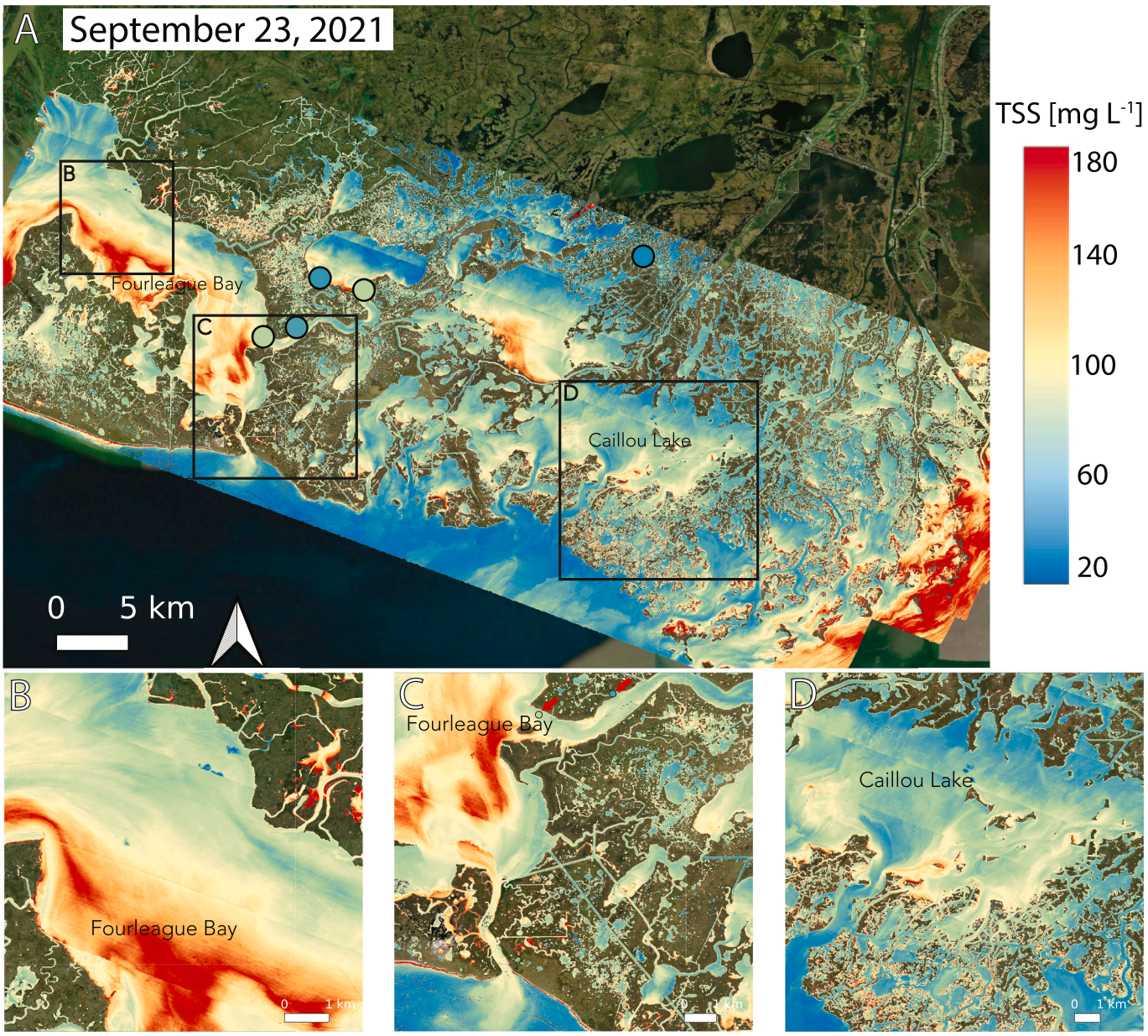

Fig. 15. TSS retrieval over the Terrebonne Basin on September 23, 2021, at low seasonal river discharge (in situ TSS 29.4–60.9 mg L^{-1}). TSS was mapped (A) over the entire basin. Insets show (B) northwestern Fourleague Bay, which receives sediment from the Atchafalaya River during high discharge; (C) southwestern Fourleague Bay, which connects to the continental shelf; and (D) Caillou Lake a shallow area mostly insulated from riverine inputs and primarily influenced by wind and tides. Points indicate the location of field sampling stations collected on September 23, 2021, and are displayed on the same color scale as the imagery (field sampling stations are highlighted with red arrows). A 5 × 5 median filter was used to address salt-and pepper artifacts from high glint in this image, most intensely for the southern-most swaths. (For interpretation of the references to colour in this figure legend, the reader is referred to the web version of this article.)

2. the Atchafalaya Basin on August 22, 2021, capturing low discharge and TSS in a river-influenced area (Fig. 13);
3. the Terrebonne Basin on April 2, 2021, capturing moderate TSS in a marsh-influenced area during high river discharge (Fig. 14); and
4. the Terrebonne Basin on September 23, 2021, capturing low TSS in a marsh-influenced area during low river discharge (Fig. 15).

Airborne TSS retrieval identified seasonal changes in TSS matching both in situ TSS and previously reported variability (Allison et al., 2012). TSS was generally higher in the spring (high river discharge) season, particularly in the river-influenced Atchafalaya Basin. These maps also featured changes in TSS distribution, across small and large channels, at spatial scales that would be impractical to measure using laboratory methods. The influence of adjacency effects contaminating pixels near the land-water boundary was pronounced in some imagery collected during the fall campaign (Appendix A5).

Imagery collected over the Atchafalaya Basin on April 1, 2021 included many small scale TSS features (spatial features 10s–100s of meters across) informative for characterizing sediment transport. High TSS (> 250 mg L^{-1}) was retrieved in the deltaic island interiors (Fig. 12D). These features were not considered artifacts of bottom reflectance (see Section 3.7.2) and indicate possible resuspension of sediment by the strong northerly winds (approximately 7.4 m/s) observed during field sampling. The winds may have also pushed water offshore causing low water level and enhanced resuspension. At the north end of the image, a plume of lower TSS water from the east branch of the intracoastal waterway (Fig. 12B) is being entrained into the main, north-south channel of the Wax Lake Outlet. The direction of the plume,

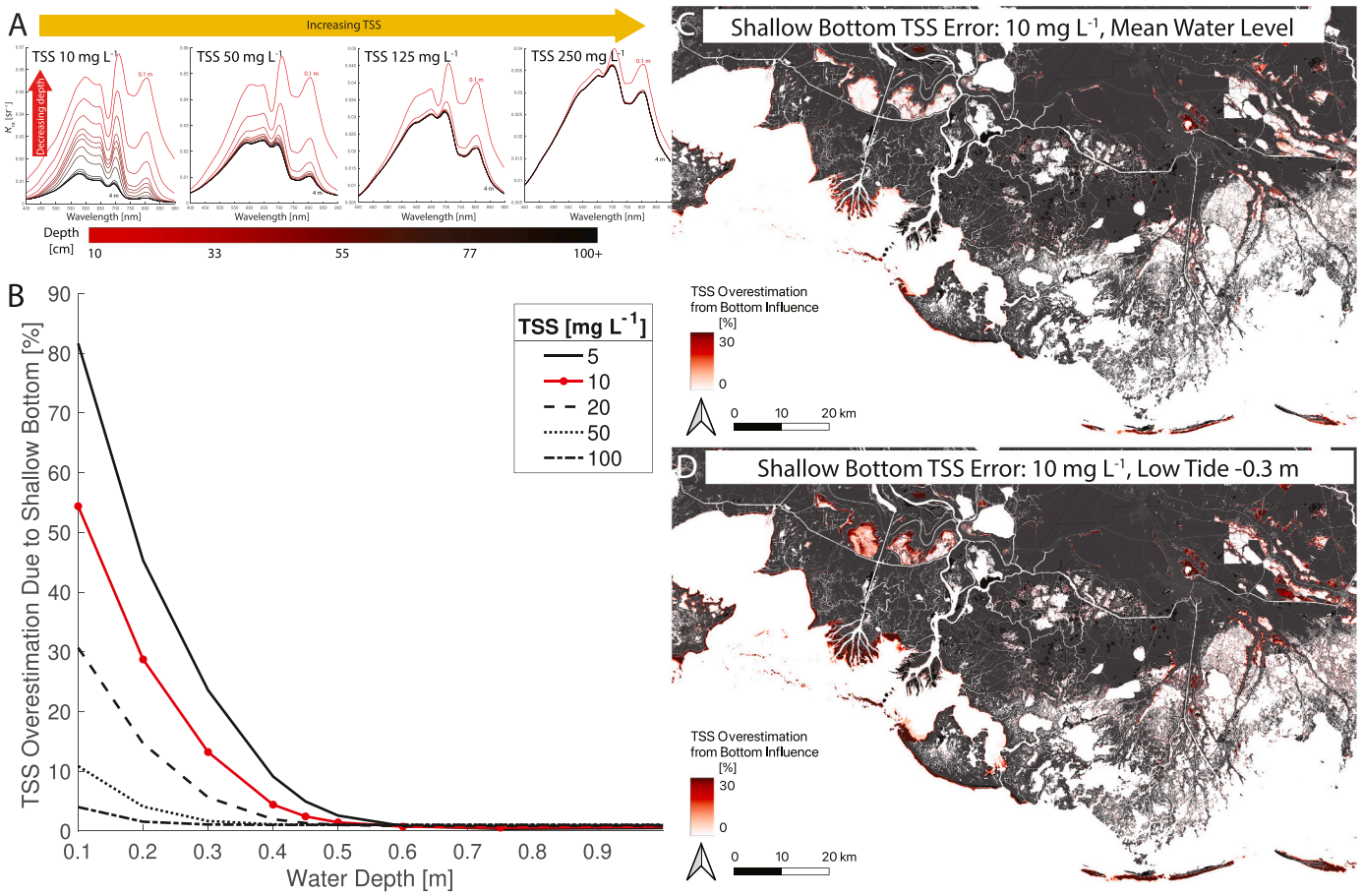

Fig. 16. HydroLight simulations of the influence of shallow bottom reflectance (dark bottom sediment) on TSS retrieval. (A) R_{rs} was modeled for a range of TSS and water depths to demonstrate the influence of bottom reflectance on contrasting waters (B) TSS was retrieved using the *Vis–NIR PLSR* algorithm from HydroLight-simulated R_{rs} and TSS overestimation in shallow waters relative to infinitely deep water was computed. Conservatively assuming 10 mg L^{-1} TSS, the depth-error relationship was applied to the DEM to identify areas where bottom reflectance causes TSS overestimation at (C) mean water level and (D) approximate low tide (MWL-0.3 m).

indicates that this portion of the intracoastal waterway, which changes flow direction (Swarzenski, 1996), was flowing from east to west at the time of imaging. Small channels were lower in TSS (Fig. 12C), especially in dead-end canals where sediment can settle out of suspension. These TSS features are useful for tracking the hydrodynamic connectivity (e.g., Wright et al., 2022) of the system and for modeling flow through small channels.

Prominent streaklines are visible across the southern portion of the image, many in areas with retrieved TSS (> 300 mg L^{-1}) greater than the maximum in situ TSS measured during the Delta-X campaign (154.5 mg L^{-1}, also on April 1). Similar features in this system have been previously interpreted as either boundaries between water masses with contrasting sediment concentrations (Ayoub et al., 2018; Salter et al., 2022) or as areas where organic surfactant slicks are spuriously interpreted as elevated TSS in the imagery (Shaw et al., 2016). Comparison of R_{rs} spectra extracted from streaklines in the April 1 AVIRIS-NG imagery with HydroLight model results for extremely turbid (TSS > 300 mg L^{-1}) waters (Appendix A8) found similar spectral shapes in the red–NIR range, supporting the explanation that the streaklines are water masses with contrasting TSS concentrations.

Mapped TSS from AVIRIS-NG imagery collected over the Atchafalaya Basin on August 22, 2021 was lower and less variable (Fig. 13) than on April 1. Streaklines were less pronounced during this lower discharge scene, though some filament-like plumes of increased TSS are visible at the edge of the delta (Fig. 13A) and in the island interiors (Fig. 13D). Flow direction in the intracoastal waterway (Fig. 13B) and decreased TSS in the small channels east of the Wax Lake outlet (Fig. 13C) are not visible in the August 22 mosaic.

Mapped TSS in the Terrebonne Basin was higher during high discharge on April 2, 2021 (Fig. 14) than during low discharge on September 23, 2021 (Fig. 15). In both seasons, many small channels and ponds in the Terrebonne Basin had lower TSS concentrations than adjacent lakes or larger channels. The highest TSS retrieved in the Terrebonne Basin imagery was on April 2 in a plume at the western end of the domain, in Fourleague Bay (Fig. 14B and C). This area, which is categorized as part of the Atchafalaya Basin, receives freshwater inputs from the Atchafalaya River during high river discharge (Perez et al., 2000; Twilley et al., 2016). The plume formed a high-TSS eddy as it entered Fourleague Bay (Fig. 14B) and was diluted through mixing with ocean water at the south end of Fourleague Bay (Fig. 14C). This high-TSS plume from the Atchafalaya River was still present in the map during low discharge on September 23, 2021 (Fig. 15A), though less widespread. Some additional areas of high TSS are visible along the southern portion of Fourleague Bay (Fig. 15C) and elsewhere in the scene (e.g., northwest of the inset for Fig. 15D) that appear to be driven by local resuspension.

TSS concentrations in the shallow marsh-influenced lakes and channels on the eastern side of the domain—away from the Atchafalaya River—were also lower on the September 23 than on the April 2. On April 2, TSS was higher in Caillou lake and had many filament-like features, particularly around a narrow, tidally flushed pass at the north end of the lake (Fig. 14D, northwest corner) that were not seen on

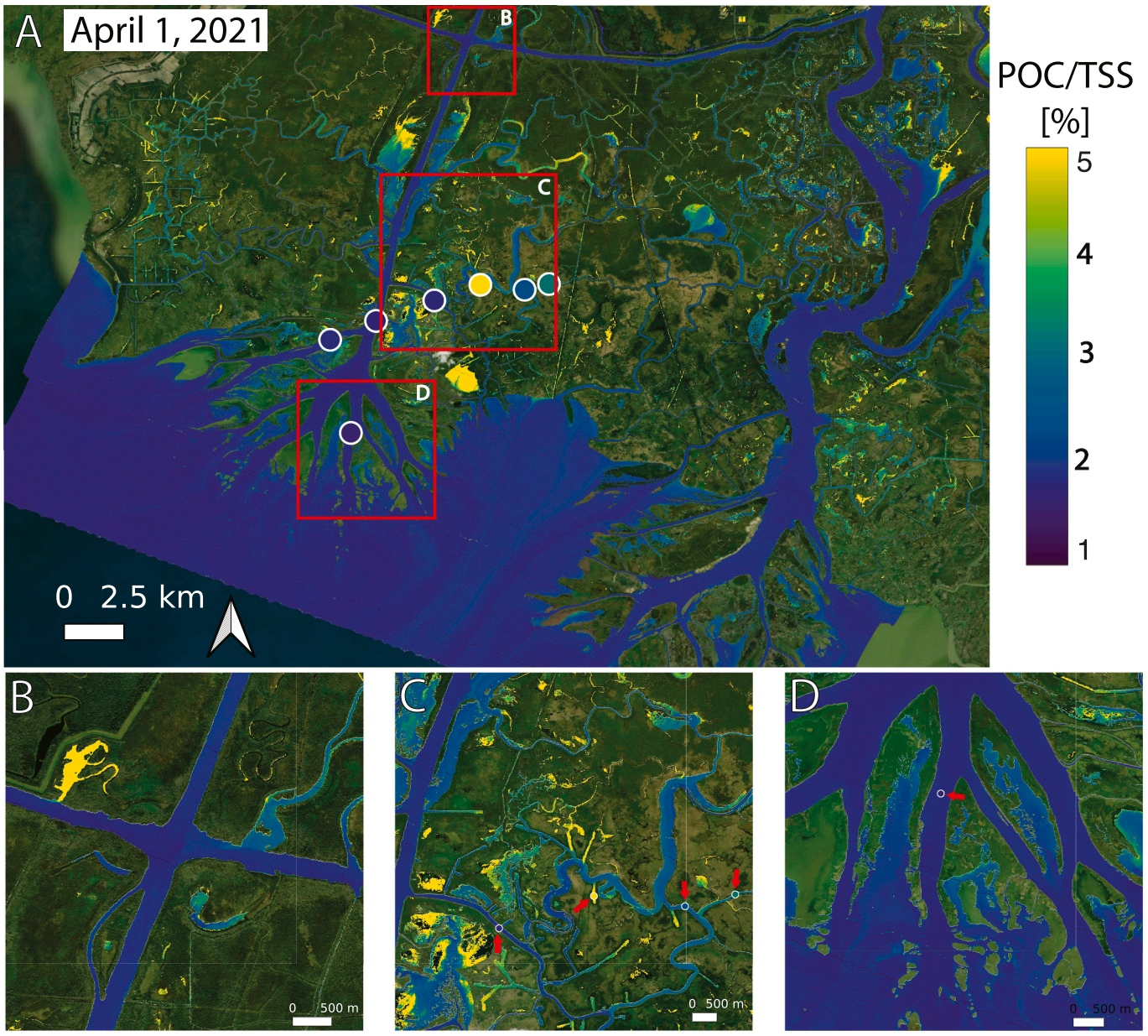

Fig. 17. POC/TSS retrieval over the Atchafalaya Basin on April 1, 2021 (In situ POC/TSS 1.58–6.16%) at high seasonal river discharge. POC/TSS was mapped (A) over the entire basin. Insets show higher resolution images of (B) the intersection of the intracoastal waterway and the Wax Lake Outlet, (C) secondary channels extending into forested freshwater marshes, and (D) the Wax Lake Delta focusing on central islands. Points indicate the location of field sampling stations collected on April 1, 2021, and are displayed on the same color scale as the imagery (field sampling stations are highlighted with red arrows). (For interpretation of the references to colour in this figure legend, the reader is referred to the web version of this article.)

September 23 (Fig. 15D). Increased TSS and higher variability may have been driven by higher spring freshwater inflow from smaller distributary channels entering the Terrebonne Basin.

3.7.2. Bottom reflectance influence on TSS

TSS retrieval can be hindered in optically shallow waters (Carder et al., 2005), where downwelling solar radiation reflects off bottom sediments, and increases measured R_{rs} across the red and NIR ranges used for TSS retrieval. Bottom-impacted and high-TSS R_{rs} spectra differ in spectral shape at other wavelengths, but universal strategies for distinguishing these effects are very challenging to develop (Carder et al., 2005). To assess the possible influence of bottom reflectance on TSS retrieved by the *Vis–NIR PLSR* algorithm, we conducted a suite of radiative transfer simulations with HydroLight using variable TSS concentrations (5–300 mg L^{-1}) and water depths (0.1–0.6 m) above a dark-sediment bottom (Fig. 16A).

Due to the rapid attenuation of light in turbid waters, bottom influence had a negligible influence on TSS retrieved from simulated R_{rs} when water depth was >0.5 m (Fig. 16B). For waters 0.1 m deep, TSS retrieval was unreliable for any TSS concentration < 300 mg L^{-1} (substantially higher than the maximum in situ TSS, 154.5 mg L^{-1}). In waters that were ≥ 0.6 m deep, retrieved TSS was negligibly impacted, almost identical to the infinitely deep case. TSS retrieval accuracy in waters 0.2, 0.3, and 0.45 m depth depended on TSS concentration, error exceeding 30% when TSS was below 125, 50, and 20 mg L^{-1} respectively. An exponential curve was fitted to the relationship between depth and TSS overestimation for waters with 10 mg L^{-1} TSS, a conservative error estimate as this is among the lowest TSS (clearest waters) measured during the field campaigns. This relationship was then applied to a bathymetry DEM (Christensen et al., 2023) at mean water level (Fig. 16C)

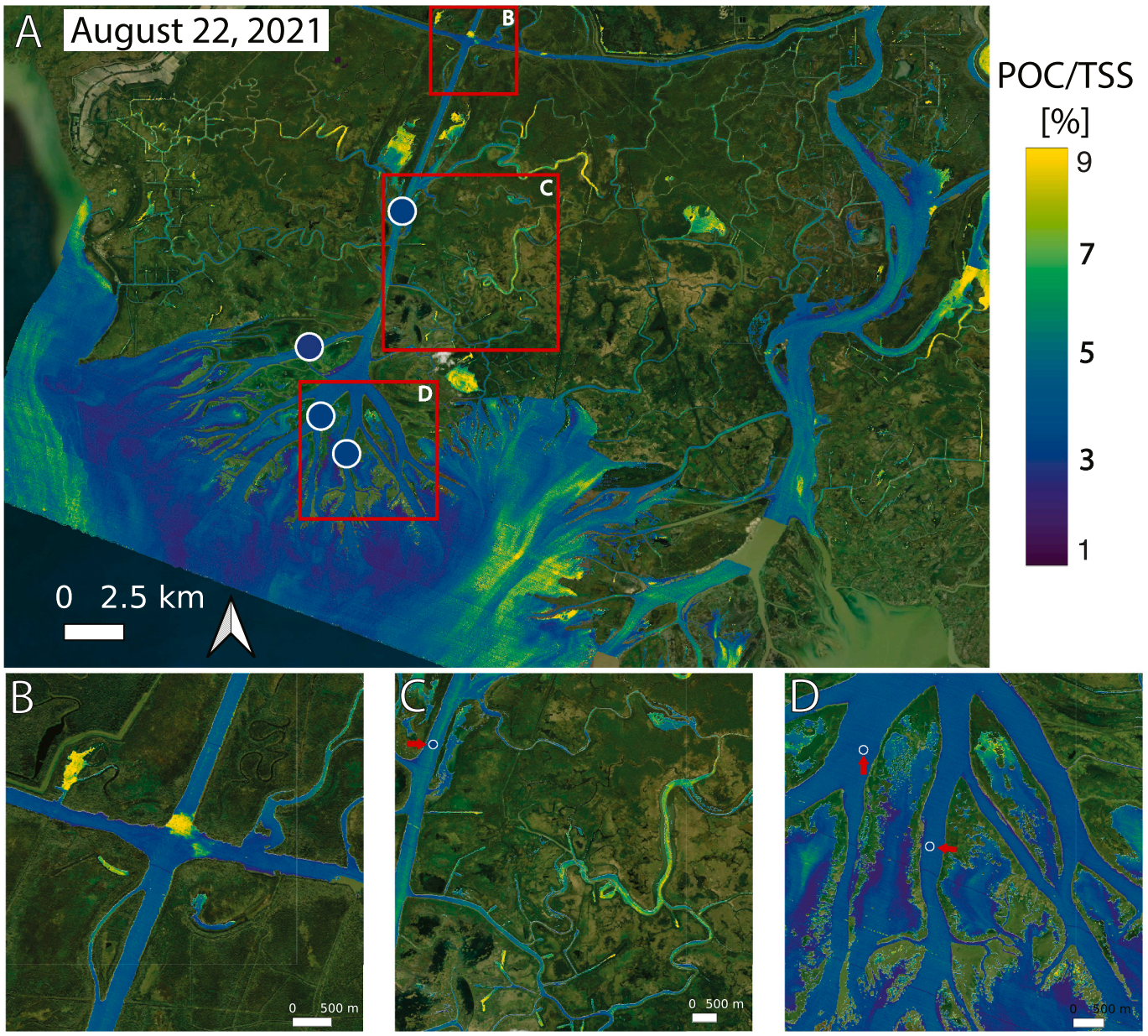

Fig. 18. POC/TSS retrieval over the Atchafalaya Basin on August 22, 2021 (In situ POC/TSS 2.19–3.40%) at low seasonal river discharge. TSS was mapped (A) over the entire basin. Insets show higher resolution images of (B) the intersection of the intracoastal waterway and the Wax Lake Outlet, (C) secondary channels extending into forested freshwater marshes, and (D) the Wax Lake Delta focusing on central islands. Points indicate the location of field sampling stations collected on August 22, 2021, and are displayed on the same color scale as the imagery (field sampling stations are highlighted with red arrows). (For interpretation of the references to colour in this figure legend, the reader is referred to the web version of this article.)

and approximate low tide conditions (Fig. 16D, mean water level−0.3 m) to map which water bodies had potential for TSS overestimation. TSS overestimation was more widespread at low tide. However, TSS overestimation was mostly <30% for both mean high water and low tide, except in areas of the Wax Lake Delta islands, some inland marshes, and the coast of some barrier islands.

3.7.3. *Seasonal trends and spatial features in POC/TSS*

POC/TSS was mapped from the same four image mosaics: the Atchafalaya Basin on April 1, 2021 (Fig. 17); the Atchafalaya Basin on August 22, 2021 (Fig. 18); the Terrebonne Basin on April 2, 2021 (Fig. 19); and the Terrebonne Basin on September 23, 2021 (Fig. 20). Mapped POC/TSS matched well with suspended POC/TSS previously measured in the Atchafalaya Basin and on the adjacent shelf (1.14–1.88%, Gordon and Goñi, 2003).

POC/TSS and TSS were often anti-correlated, particularly in the Atchafalaya Basin during high discharge, where the highest TSS concentrations were associated with mineral loading from riverine inputs. POC/TSS on April 1 was low (mostly ≤ 2%) with low variability. The spatial distribution of POC/TSS on April 1, included streaklines (Fig. 17A and D), where POC/TSS exiting main channels of the delta and on the downstream side of delta islands was lower. POC/TSS in the fall campaign also had some streakline features, which were most pronounced in the area between Wax Lake Delta and the Atchafalaya River delta (east of inset for Fig. 18 D). POC/TSS was higher in small channels and other low-energy environments in both the spring and fall (Fig. 17C and 18C), indicating a gradient from mineral particles suspended by currents to sediment with more organic-rich detrital and algal particles. POC/TSS at validation stations on April 1 and August 22 matched well to POC/TSS retrieved from the AVIRIS-NG imagery, though August 22

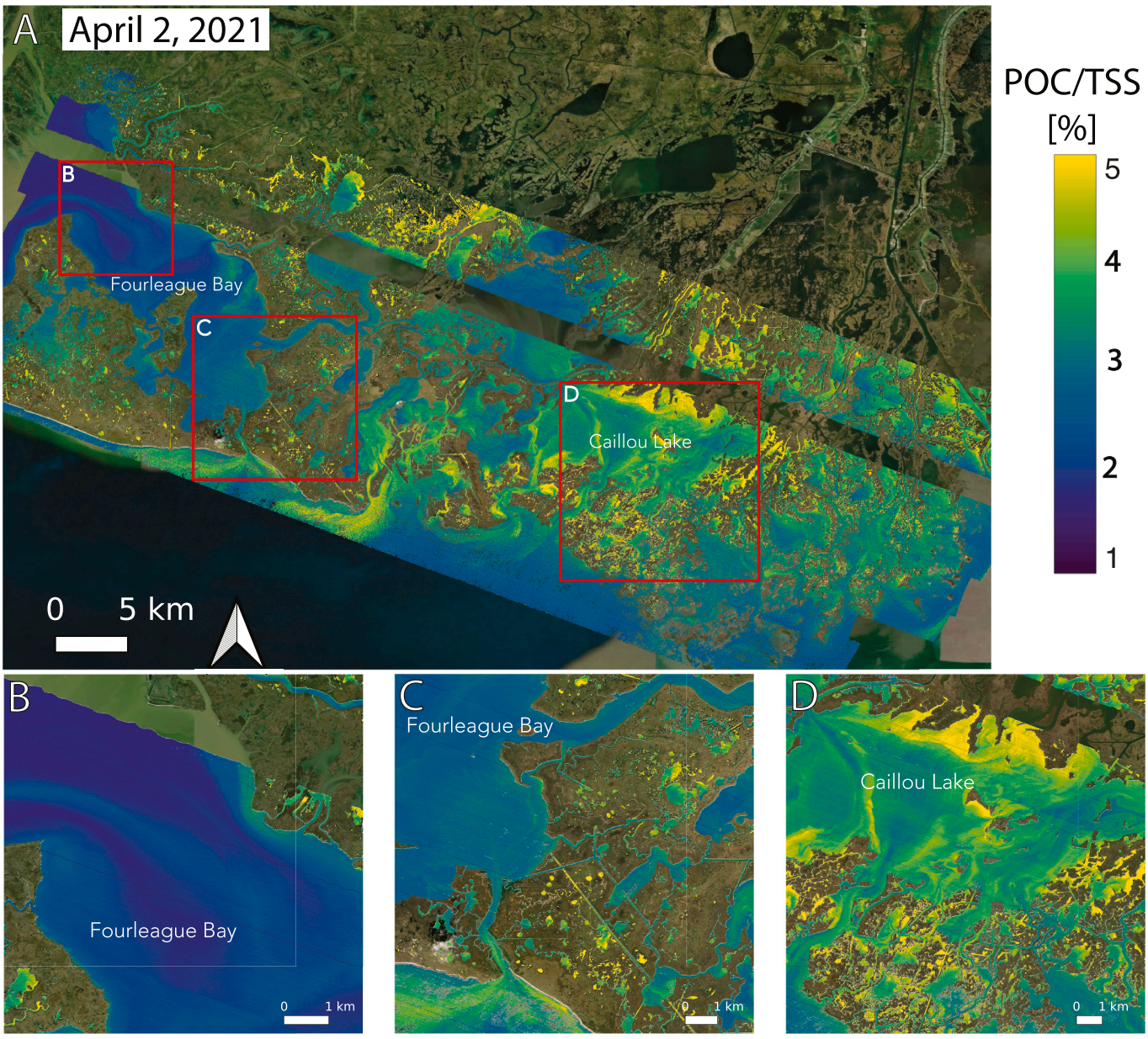

Fig. 19. POC/TSS retrieval over the Terrebonne Basin on April 2, 2021, at high seasonal river discharge. POC/TSS was mapped (A) over the entire basin. Insets show (B) northwestern Fourleague Bay, which receives sediment from the Atchafalaya River during high discharge; (C) southeastern Fourleague Bay, which connects to the continental shelf; and (D) Caillou Lake a shallow area mostly insulated from riverine inputs and primarily influenced by wind and tides.

validation stations were only collected in main channels and did not represent the full range of conditions present in the image.

The injection of mineral-rich particles from the Atchafalaya River was visible in a plume of low POC/TSS water entering Fourleague Bay in the April 2 (Fig. 19A and B) and September 23 (Fig. 20A and B) mosaics. This plume covers an extent similar to the plume of high TSS water visible in the TSS map from April 2 (Fig. 12A). This high TSS low POC/TSS plume identifies an area high in river-influenced sediment that is different in composition from the locally resuspended particles in Terrebonne Bay (Fig. 19B). The April 2 mosaic also includes plumes of high POC/TSS particles from the coastal marsh-estuary system to adjacent bays (south and east of Fig. 19C. Shallow sheltered areas on the margins of Caillou Lake in the eastern Terrebonne Basin (Fig. 19D) were relatively high in POC/TSS likely due to low riverine inputs and mineral resuspension relative to primary productivity and detrital organic matter.

POC/TSS across the Terrebonne Basin was highest during the fall campaign. POC/TSS was high in shallow waters of Caillou Lake and north of Caillou Lake (north of Fig. 20D). Plumes of low-POC/TSS water were visible along the north shore of Fourleague Bay with plumes high-POC/TSS water along the southwest shore (Fig. 20B). POC/TSS was accurately retrieved on September 23 across a wide range of concentrations, though some residual sunglint "salt-and-pepper" artifacts are visible, particularly at the southern end of the image (a 5 × 5 median filter was applied to the POC/TSS map to correct some of these artifacts).

POC/TSS was higher in the Terrebonne Basin than in the Atchafalaya Basin during both field campaigns, which matched prior findings of higher phytoplankton biomass in the Terrebonne Basin (Sweet et al., 2022). Though both basins had higher POC/TSS in the fall than in the spring, the Terrebonne Basin had a larger increase in POC/TSS from the April 2, 2021 mosaic from spring field campaign (Fig. 19) to the September 23, 2021 mosaic from the fall field campaign (Fig. 20) than was observed in the Atchafalaya Basin. The large seasonal increase in carbon content in the Terrebonne Basin was matched by an increase in

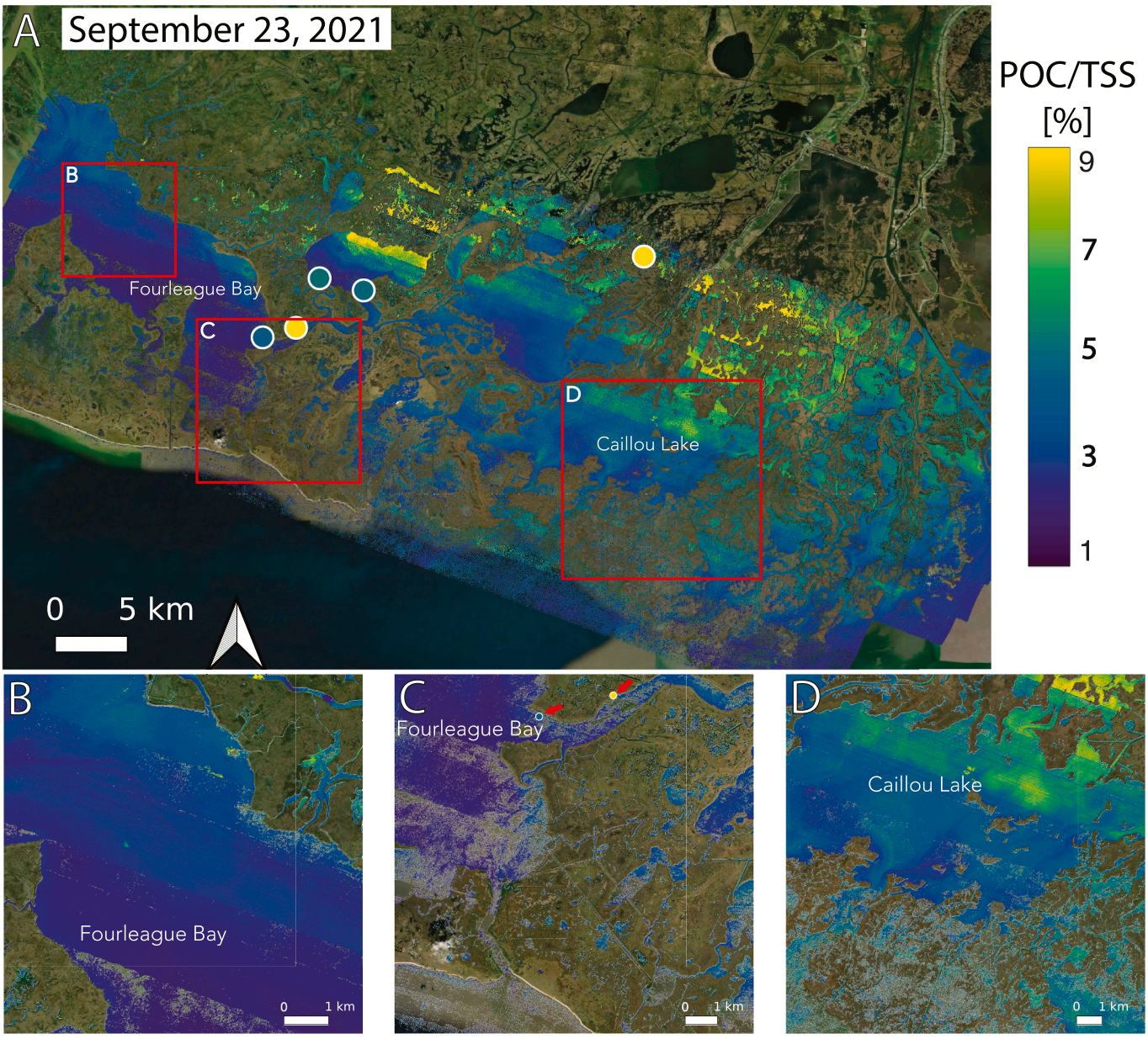

Fig. 20. POC/TSS retrieval over the Terrebonne Basin on September 23, 2021, at low seasonal river discharge (in situ POC/TSS 4.6–12.9%). POC/TSS was mapped (A) over the entire basin. Insets show (B) northwestern Fourleague Bay, which receives sediment from the Atchafalaya River during high discharge; (C) southwestern Fourleague Bay, which connects to the continental shelf; and (D) Caillou Lake a shallow area mostly insulated from riverine inputs and primarily influenced by wind and tides. Points indicate the location of field sampling stations collected on September 23, 2021, and are displayed on the same color scale as the imagery (field sampling stations are highlighted with red arrows). A 5 × 5 median filter was used to address salt-and pepper artifacts from high glint in this image, most intense in the southern-most swaths. (For interpretation of the references to colour in this figure legend, the reader is referred to the web version of this article.)

$a_p(676)$ line height measured in situ between the spring and fall campaigns (Fig. 4F), indicating that the POC/TSS increase was driven by autochthonous primary production during the fall campaign. The Terrebonne basin also received much smaller inputs of mineral-rich waters from the Atchafalaya River allowing organic particles to comprise a larger fraction of TSS.

4. Concluding remarks

Maps of TSS and POC/TSS retrieved from airborne imaging spectroscopy proved suitable for sediment monitoring, meeting the criteria presented for suitability: 1. the maps accurately retrieved parameters across a range of concentrations, outperforming existing approaches for TSS, and 2. the maps resolved real spatial and temporal variability with minimal artifacts. The *Vis–NIR PLSR* algorithm retrieved TSS accurately across a wide range of concentrations from extremely turbid riverine and nearshore settings in the Mississippi River Deltaic Plain to Gulf of Mexico continental-shelf waters. The extremely turbid nearshore waters encountered in the Delta-X campaigns are under-represented in existing calibration datasets, and the accurate retrieval of TSS and POC/TSS in waters ranging from relatively clear coastal waters to extremely turbid nearshore waters offers clear advantages for coastal imaging-spectroscopy-based monitoring (e.g., NASA SBG and GLIMR missions). Mapped TSS distributions resolved seasonal shifts in TSS concentration, as well as streaklines, and concentrations in narrow channels, capturing spatial features indicative of sediment sourcing and transport processes. We also identified circumstances that hindered TSS retrieval, where additional caution should be taken when using TSS maps. We mapped

water bodies where retrieved TSS was spuriously increased by the influence of bottom reflectance, which mostly occurred in waters ≤0.5 m depth. Our analysis demonstrated the reliability of TSS maps derived from imaging spectroscopy, with residual atmospheric correction errors and adjacency effects as the most significant remaining error sources for high aerosol loads (especially for TSS < 40 mg L^{-1}).

The feasibility of remotely retrieving particle properties that influence sediment transport and accretion—composition and size—was explored. A PLSR-based algorithm utilizing hyperspectral Vis–NIR reflectance was also able to accurately retrieve POC/TSS. Accurate POC/TSS retrieval was validated using in situ and AVIRIS-NG-derived matchup spectra. Mapped POC/TSS quantified seasonal and between-basin differences in carbon content, matching previously measured riverine, mineral-bound organic matter (Gordon and Goñi, 2003) in the Atchafalaya Basin and previously measured phytoplankton dynamics in the Terrebonne Basin (Sweet et al., 2022). Particle mean diameter was also compared to a range of environmental parameters and optical characteristics, but—unlike in previous studies—mean diameter did not have clear optical proxies in this system. Previous research (Buonassissi and Dierssen, 2010) has identified differences in the size-backscattering relationships between systems. The presence of heterogeneous particles with complex relationships between particle size, geometry, and composition likely complicated the relationship between size and IOPs, contributing to the difficulty in retrieving particle diameter.

Operational atmospheric correction and field validation datasets for future hyperspectral, ocean color missions will facilitate the production of usable products. The spectral downsampling analysis presented in this work demonstrated the advantages of high spectral resolution R_{rs} spectra for retrieving TSS and POC/TSS, and likely for other constituent compositional properties which exert a subtle influence on R_{rs} spectral shape. The algorithms presented in this work are applicable to upcoming satellite imaging spectroradiometers, offering improved retrieval of suspended sediment characteristics in turbid coastal waters. We anticipate their application on repeat satellite imaging spectroscopy will provide frequent and long-term monitoring of particles in the nearshore coastal zone. While the Delta-X AVIRIS-NG imagery provided snapshots of TSS distribution and particle carbon content that were suitable for this feasibility study, the temporal coverage expected from the GLIMR and SBG missions will facilitate the continuous monitoring of this vulnerable coastline. Libraries of repeat imaging spectroscopy will help identify environmental forcing and temporal trends in TSS and particulate carbon content on inter-annual, seasonal, and weekly timescales. The application of algorithms to repeat imagery will also help capture a representative range of TSS distributions and compositions in coastal waters, allowing for the parametrization of more accurate sediment and carbon budgets, with benefits for communities relying upon these vulnerable coastlines.

CRediT authorship contribution statement

Joshua P. Harringmeyer: Conceptualization, Methodology, Validation, Formal analysis, Investigation, Writing – original draft, Writing – review & editing, Visualization. **Nilotpal Ghosh:** Investigation, Writing – review & editing. **Matthew W. Weiser:** Investigation, Writing – review & editing. **David R. Thompson:** Investigation, Writing – review & editing. **Marc Simard:** Writing – review & editing, Supervision, Project administration, Funding acquisition. **Steven E. Lohrenz:** Investigation, Data curation, Writing – review & editing. **Cédric G. Fichot:** Conceptualization, Methodology, Formal analysis, Investigation, Resources, Data curation, Writing – review & editing, Supervision, Funding acquisition.

Declaration of Competing Interest

The authors declare that they have no known competing financial interests or personal relationships that could have appeared to influence the work reported in this paper.

Data availability

Data collected during the Delta-X investigation are freely available at the ORNL DAAC: https://daac.ornl.gov/cgi-bin/dataset_lister.pl?p=41

Acknowledgments

This work (Delta-X mission) was funded by the NASA Science Mission Directorate's Earth Science Division through the Earth Venture Suborbital-3 Program (NNH17ZDA001N-EVS3). Work was also supported by a NASA FINESST grant 80NSSC20K1648 to graduate student JH (PI CF) as well funding from NASA (NNX14AO73G and 80LARC21DA002) and the National Science Foundation (OCE-0752254) to SL. A portion of this research took place at the Jet Propulsion Laboratory, California Institute of Technology, under contract with the National Aeronautics and Space Administration. We would like to thank Luca Cortese and Hope Vanderhider for their assistance during field sampling. We also thank Xiaohui Zhu for contributing the spectrophotometric analyses of CDOM absorption coefficient used for radiative transfer modeling in this study. We are most grateful to Emmanuel Boss for lending the WetLABS ECO bb2FL instrument used in this study. We thank Sarah Epps for contributing to the GulfCarbon TSS data collection and analysis. Finally, we would also like to thank our colleagues at Louisiana State University, Andre Rovai, John O'Connor, and Robert Twilley for their invaluable assistance during the field campaigns.

Appendix A. Supplementary data

Supplementary data to this article can be found online at https://doi.org/10.1016/j.rse.2023.113943.

References

Allison, M.A., Demas, C.R., Ebersole, B.A., Kleiss, B.A., Little, C.D., Meselhe, E.A., Powell, N.J., Pratt, T.C., Vosburg, B.M., 2012. A water and sediment budget for the lower Mississippi-Atchafalaya River in flood years 2008-2010: implications for sediment discharge to the oceans and coastal restoration in Louisiana. J. Hydrol. (Amst.) 432–433, 84–97. https://doi.org/10.1016/j.jhydrol.2012.02.020.

Arlot, S., Celisse, A., 2010. A survey of cross-validation procedures for model selection. Stat. Surv. 4, 40–79. https://doi.org/10.1214/09-SS054.

Aurin, D.A., Dierssen, H.M., 2012. Advantages and limitations of ocean color remote sensing in CDOM-dominated, mineral-rich coastal and estuarine waters. Remote Sens. Environ. 125, 181–197. https://doi.org/10.1016/j.rse.2012.07.001.

Ayoub, F., Jones, C.E., Lamb, M.P., Holt, B., Shaw, J.B., Mohrig, D., Wagner, W., 2018. Inferring surface currents within submerged, vegetated deltaic islands and wetlands from multi-pass airborne SAR. Remote Sens. Environ. 212, 148–160. https://doi.org/10.1016/j.rse.2018.04.035.

Balasubramanian, S.V., Pahlevan, N., Smith, B., Binding, C., Schalles, J., Loisel, H., Gurlin, D., Greb, S., Alikas, K., Randla, M., Bunkei, M., Moses, W., Nguyễn, H., Lehmann, M.K., O'Donnell, D., Ondrusek, M., Han, T.H., Fichot, C.G., Moore, T., Boss, E., 2020. Robust algorithm for estimating total suspended solids (TSS) in inland and nearshore coastal waters. Remote Sens. Environ. 246, 111768 https://doi.org/10.1016/j.rse.2020.111768.

Barbier, E.B., Hacker, S.D., Kennedy, C., Koch, E.W., Stier, A.C., Silliman, B.R., 2011. The value of estuarine and coastal ecosystem services. Ecol. Monogr. 81, 169–193. https://doi.org/10.1890/10-1510.1.

Bianchi, T.S., Galler, J.J., Allison, M.A., 2007. Hydrodynamic sorting and transport of terrestrially derived organic carbon in sediments of the Mississippi and Atchafalaya Rivers. Estuar. Coast. Shelf Sci. 73, 211–222. https://doi.org/10.1016/j.ecss.2007.01.004.

Bianchi, T.S., Wysocki, L.A., Schreiner, K.M., Filley, T.R., Corbett, D.R., Kolker, A.S., 2011. Sources of terrestrial organic carbon in the Mississippi plume region: evidence for the importance of coastal marsh inputs. Aquat. Geochem. 17, 431–456. https://doi.org/10.1007/s10498-010-9110-3.

Bilotta, G.S., Brazier, R.E., 2008. Understanding the influence of suspended solids on water quality and aquatic biota. Water Res. 42, 2849–2861. https://doi.org/10.1016/j.watres.2008.03.018.

Blum, M.D., Roberts, H.H., 2009. Drowning of the Mississippi Delta due to insufficient sediment supply and global sea-levelrise. Nat. Geosci. 2, 488–491. https://doi.org/10.1038/ngeo553.

Boss, E., Pegau, W.S., Gardner, W.D., Zaneveld, J.R.V., Barnard, A.H., Twardowski, M.S., Chang, G.C., Dickey, T.D., 2001. Spectral particulate attenuation and particle size

distribution in the bottom boundary layer of a continental shelf. J. Geophys. Res. Oceans 106, 9509–9516. https://doi.org/10.1029/2000jc900077.
Boss, E., Sherwood, C.R., Hill, P., Milligan, T., 2018. Advantages and limitations to the use of optical measurements to study sediment properties. Appl. Sci. (Switzerland) 8. https://doi.org/10.3390/app8122692.
Bowers, D.G., Hill, P.S., Braithwaite, K.M., 2014. The effect of particulate organic content on the remote sensing of marine suspended sediments. Remote Sens. Environ. 144, 172–178. https://doi.org/10.1016/j.rse.2014.01.005.
Bulgarelli, B., Zibordi, G., 2018. On the detectability of adjacency effects in ocean color remote sensing of mid-latitude coastal environments by SeaWiFS, MODIS-A, MERIS, OLCI, OLI and MSI. Remote Sens. Environ. 209, 423–438. https://doi.org/10.1016/j.rse.2017.12.021.
Buonassissi, C.J., Dierssen, H.M., 2010. A regional comparison of particle size distributions and the power law approximation in oceanic and estuarine surface waters. J. Geophys. Res. Oceans 115, 1–12. https://doi.org/10.1029/2010JC006256.
Candela, A., Edelson, K., Gierach, M.M., Thompson, D.R., Woodward, G., Wettergreen, D., 2021. Using remote sensing and in situ measurements for efficient mapping and optimal sampling of coral reefs. Front. Mar. Sci. 8, 1–17. https://doi.org/10.3389/fmars.2021.689489.
Carder, K.L., Cannizzaro, J.P., Lee, Z., 2005. Ocean color algorithms in optically shallow waters: limitations and improvements. Remote Sens. Coast. Ocean. Environ. 5885, 588506 https://doi.org/10.1117/12.615039.
Chakraborty, S., 2013. Phytoplankton Community Distribution and Light Absorption Properties in the Northern Gulf of Mexico. ProQuest Dissertations and Theses. United States - Mississippi.
Chapman, J.W., Thompson, D.R., Helmlinger, M.C., Bue, B.D., Green, R.O., Eastwood, M. L., Geier, S., Olson-Duvall, W., Lundeen, S.R., 2019. Spectral and radiometric calibration of the next generation airborne visible infrared spectrometer (AVIRIS-NG). Remote Sens. 11, 2129. https://doi.org/10.3390/RS11182129.
Chaves, J.E., Cetinić, I., Dall'Olmo, G., Estapa, M., Gardner, W., Goñi, M., Graff, J.R., Hernes, P., Lam, P.J., Liu, Z., Lomas, M.W., Mannino, A., Novak, M.G., Turnewitsch, R., Werdell, P.J., Westberry, T.K., 2021. IOCCG protocol series (2021). In: Particulate Organic Matter Sampling and Measurement Protocols: Consensus Towards Future Ocean Color Missions, IOCCG Ocean Optics and Biogeochemistry Protocols for Satellite Ocean Colour Sensor Validation. Dartmouth, NS, Canada.
Christensen, A.L., Denbina, M.W., Simard, M., 2023. Delta-X: Digital Elevation Model, MRD, LA, USA, 2021. https://doi.org/10.3334/ORNLDAAC/2181.
Cortese, L., Fagherazzi, S., 2022. Fetch and distance from the bay control accretion and erosion patterns in Terrebonne marshes (Louisiana, USA). Earth Surf. Process. Landf. 47, 1455–1465. https://doi.org/10.1002/ESP.5327.
Cortese, L., Donatelli, C., Zhang, X., Nghiem, J.A., Simard, M., Jones, C.E., Denbina, M., Fichot, C.G., Harringmeyer, J.P., Fagherazzi, S., 2023. Coupling numerical models of deltaic wetlands with AirSWOT, UAVSAR, and AVIRIS-NG remote sensing data, Biogeosci. Discuss. [preprint], https://doi.org/10.5194/bg-2023-108, in review, 2023.
Costanza, R., de Groot, R., Sutton, P., van der Ploeg, S., Anderson, S.J., Kubiszewski, I., Farber, S., Turner, R.K., 2014. Changes in the global value of ecosystem services. Glob. Environ. Chang. 152–158 https://doi.org/10.1016/j.gloenvcha.2014.04.002.
Dierssen, H.M., Chlus, A., Russell, B., 2015. Hyperspectral discrimination of floating mats of seagrass wrack and the macroalgae Sargassum in coastal waters of greater Florida bay using airborne remote sensing. Remote Sens. Environ. 167, 247–258. https://doi.org/10.1016/j.rse.2015.01.027.
Dierssen, H.M., Ackleson, S.G., Joyce, K.E., Hestir, E.L., Castagna, A., Lavender, S., McManus, M.A., 2021. Living up to the hype of hyperspectral aquatic remote sensing: science, resources and outlook. Front. Environ. Sci. 9, 1–26. https://doi.org/10.3389/fenvs.2021.649528.
Dogliotti, A.I., Ruddick, K.G., Nechad, B., Doxaran, D., Knaeps, E., 2015. A single algorithm to retrieve turbidity from remotely-sensed data in all coastal and estuarine waters. Remote Sens. Environ. 156, 157–168. https://doi.org/10.1016/j.rse.2014.09.020.
Doxaran, D., Leymarie, E., Nechad, B., Dogliotti, A., Ruddick, K., Gernez, P., Knaeps, E., 2016. Improved correction methods for field measurements of particulate light backscattering in turbid waters. Opt. Express 24, 3615. https://doi.org/10.1364/oe.24.003615.
Edmonds, D.A., Voller, V.R., Viparelli, E., Parker, G., Twilley, R.R., Paola, C., Kim, W., Mohrig, D., 2010. Natural processes in delta restoration: application to the Mississippi Delta. Annu. Rev. Mar. Sci. 3, 67–91. https://doi.org/10.1146/annurev-marine-120709-142856.
Epps, S., 2018. The feasibility of using inherent optical properties and the apparent optical property remote sensing reflectance to estimate suspended particulate matter, particularly for use in airborne hydrographic surveys. University of Southern Mississippi, Dissertations.
Evers-King, H., Martinez-Vicente, V., Brewin, R.J.W., Dall'Olmo, G., Hickman, A.E., Jackson, T., Kostadinov, T.S., Krasemann, H., Loisel, H., Röttgers, R., Roy, S., Stramski, D., Thomalla, S., Platt, T., Sathyendranath, S., 2017. Validation and intercomparison of ocean color algorithms for estimating particulate organic carbon in the oceans. Front. Mar. Sci. 4, 1–20. https://doi.org/10.3389/fmars.2017.00251.
Farrés, M., Platikanov, S., Tsakovski, S., Tauler, R., 2015. Comparison of the variable importance in projection (VIP) and of the selectivity ratio (SR) methods for variable selection and interpretation. J. Chemom. 29, 528–536. https://doi.org/10.1002/cem.2736.
Fichot, C.G., Harringmeyer, J., 2022a. Delta-X: In Situ Water Surface Reflectance, Atchafalaya and Terrebonne Basins, 2021. https://doi.org/10.3334/ORNLDAAC/2076.
Fichot, C.G., Harringmeyer, J., 2022b. Delta-X: In situ Beam Attenuation and Particle Size from LISST-200X, 2021. https://doi.org/10.3334/ORNLDAAC/2077.
Fichot, C.G., Lohrenz, S.E., Benner, R., 2014. Pulsed, cross-shelf export of terrigenous dissolved organic carbon to the Gulf of Mexico. J. Geophys. Res. Oceans 119, 1176–1194. https://doi.org/10.1002/2013JC009424.
Fichot, C.G., Downing, B.D., Bergamaschi, B.A., Windham-Myers, L., Marvin-Dipasquale, M., Thompson, D.R., Gierach, M.M., 2016. High-resolution remote sensing of water quality in the San Francisco Bay-Delta estuary. Environ. Sci. Technol. 50, 573–583. https://doi.org/10.1021/acs.est.5b03518.
Fichot, C.G., Ghosh, N., Harringmeyer, J., Weiser, M., 2022a. Delta-X: Total Suspended Solids Concentration across MRD, LA, USA, 2021. https://doi.org/10.3334/ORNLDAAC/2075.
Fichot, C.G., Ghosh, N., Harringmeyer, J., Weiser, M., 2022b. Delta-X: Particulate Organic Carbon Concentration from Water Samples, MRD, LA, 2021. https://doi.org/10.3334/ORNLDAAC/2073.
Fichot, C.G., Harringmeyer, J., Weiser, M., 2022c. Delta-X: In Situ Water Quality Indicators across MRD, LA, USA, 2021. https://doi.org/10.3334/ORNLDAAC/2080.
Ford, R.T., Vodacek, A., 2020. Determining improvements in Landsat spectral sampling for inland water quality monitoring. Sci. Remote Sens. 1, 100005 https://doi.org/10.1016/j.srs.2020.100005.
Frouin, R.J., Franz, B.A., Ibrahim, A., Knobelspiesse, K., Ahmad, Z., Cairns, B., Chowdhary, J., Dierssen, H.M., Tan, J., Dubovik, O., Huang, X., Davis, A.B., Kalashnikova, O., Thompson, D.R., Remer, L.A., Boss, E., Coddington, O., Deschamps, P.Y., Gao, B.C., Gross, L., Hasekamp, O., Omar, A., Pelletier, B., Ramon, D., Steinmetz, F., Zhai, P.W., 2019. Atmospheric correction of satellite ocean-color imagery during the PACE era. Front. Earth Sci. (Lausanne) 7, 1–43. https://doi.org/10.3389/feart.2019.00145.
Galy, V., Peucker-Ehrenbrink, B., Eglinton, T., 2015. Global carbon export from the terrestrial biosphere controlled by erosion. Nature 521, 204–207. https://doi.org/10.1038/nature14400.
Giosan, L., Syvitski, J., Constantinescu, S., Day, J., 2014. Protect the world's deltas. Nature 516, 31–33.
Goñi, M.A., Ruttenberg, K.C., Eglinton, T.I., 1998. A reassessment of the sources and importance of land-derived organic matter in surface sediments from the Gulf of Mexico. Geochim. Cosmochim. Acta 62, 3055–3075. https://doi.org/10.1016/S0016-7037(98)00217-8.
Gordon, E.S., Goñi, M.A., 2003. Sources and distribution of terrigenous organic matter delivered by the Atchafalaya River to sediments in the northern Gulf of Mexico. Geochim. Cosmochim. 67, 2359–2375. https://doi.org/10.1016/S0016-7037(02)01412-6.
Gordon, E.S., Goñi, M.A., Roberts, Q.N., Kineke, G.C., Allison, M.A., 2001. Organic matter distribution and accumulation on the inner Louisiana shelf west of the Atchafalaya River. Cont. Shelf Res. 21, 1691–1721. https://doi.org/10.1016/S0278-4343(01)00021-8.
Greenberg, E., Thompson, D.R., Jensen, D.J., Townsend, P.A., Queally, N., Chlus, A., Fichot, C.G., Harringmeyer, J., Simard, M., 2022. An improved scheme for correcting remote spectral surface reflectance simultaneously for terrestrial BRDF and water-surface sunglint in coastal environments. J. Geophys. Res. Biogeosci. 1–21 https://doi.org/10.1029/2021jg006712.
Harringmeyer, J.P., Kaiser, K., Thompson, D.R., Gierach, M.M., Cash, C.L., Fichot, C.G., 2021. Detection and sourcing of CDOM in urban coastal waters with UV-visible imaging spectroscopy. Front. Environ. Sci. 9, 1–21. https://doi.org/10.3389/fenvs.2021.647966.
Hedges, J.I., Baldock, J.A., Gelinas, Y., Lee, C., Peterson, M., Wakeham, S.G., 2001. Evidence for non-selective preservation of organic matter in sinking marine particles. Nature 409, 801–804.
Jensen, D., Simard, M., Cavanaugh, K., Sheng, Y., Fichot, C.G., Pavelsky, T., Twilley, R., 2019. Improving the transferability of suspended solid estimation in wetland and deltaic waters with an empirical hyperspectral approach. Remote Sens. 11, 1629. https://doi.org/10.3390/rs11131629.
Jiang, D., Matsushita, B., Yang, W., 2020. A simple and effective method for removing residual reflected skylight in above-water remote sensing reflectance measurements. ISPRS J. Photogramm. Remote Sens. 165, 16–27. https://doi.org/10.1016/j.isprsjprs.2020.05.003.
Jiang, D., Matsushita, B., Pahlevan, N., Gurlin, D., Lehmann, M.K., Fichot, C.G., Schalles, J., Loisel, H., Binding, C., Zhang, Y., Alikas, K., Kangro, K., Uusõue, M., Ondrusek, M., Greb, S., Moses, W.J., Lohrenz, S., O'Donnell, D., 2021. Remotely estimating total suspended solids concentration in clear to extremely turbid waters using a novel semi-analytical method. Remote Sens. Environ. 258 https://doi.org/10.1016/j.rse.2021.112386.
Khelifa, A., Hill, P.S., 2006. Models for effective density and settling velocity of flocs. J. Hydraul. Res. 44, 390–401. https://doi.org/10.1080/00221686.2006.9521690.
Kolker, A.S., Li, C., Walker, N.D., Pilley, C., Ameen, A.D., Boxer, G., Ramatchandirane, C., Ullah, M., Williams, K.A., 2014. The impacts of the great Mississippi/Atchafalaya River flood on the oceanography of the Atchafalaya shelf. Cont. Shelf Res. 86, 17–33. https://doi.org/10.1016/j.csr.2014.04.023.
Kostadinov, T.S., Siegel, D.A., Maritorena, S., 2009. Retrieval of the particle size distribution from satellite ocean color observations. J. Geophys. Res. Oceans 114, 1–22. https://doi.org/10.1029/2009JC005303.
Le, C., Lehrter, J.C., Hu, C., MacIntyre, H., Beck, M.W., 2017. Satellite observation of particulate organic carbon dynamics on the Louisiana continental shelf. J. Geophys. Res. Oceans 122, 555–569. https://doi.org/10.1038/175238c0.
Lee, Z., Carder, K.L., Arnone, R.A., 2007. Deriving inherent optical properties from water color: a multiband quasi-analytical algorithm for optically deep waters. Appl. Opt. 41, 5755. https://doi.org/10.1364/ao.41.005755.

Lee, Z., Lubac, B., Werdell, J., 2014. Update of the Quasi-Analytical Algorithm (QAA_v6). International Ocean Color Group Software Report.
Lin, J., Lyu, H., Miao, S., Pan, Y., Wu, Z., Li, Y., Wang, Q., 2018. A two-step approach to mapping particulate organic carbon (POC) in inland water using OLCI images. Ecol. Indic. 90, 502–512. https://doi.org/10.1016/j.ecolind.2018.03.044.
Liu, Z., Fagherazzi, S., Cui, B., 2021a. Success of coastal wetlands restoration is driven by sediment availability. Commun. Earth Environ. 2 https://doi.org/10.1038/S43247-021-00117-7.
Liu, H., Li, Q., Bai, Y., Yang, C., Wang, J., Zhou, Q., Hu, S., Shi, T., Liao, X., Wu, G., 2021b. Improving satellite retrieval of oceanic particulate organic carbon concentrations using machine learning methods. Remote Sens. Environ. 256, 112316 https://doi.org/10.1016/j.rse.2021.112316.
Lyu, H., Wang, Y., Jin, Q., Shi, L., Li, Y., Wang, Q., 2017. Developing a semi-analytical algorithm to estimate particulate organic carbon (POC) levels in inland eutrophic turbid water based on MERIS images: A case study of Lake Taihu. Int. J. Appl. Earth Obs. Geoinf. 62, 69–77. https://doi.org/10.1016/j.jag.2017.06.001.
Martinez-Vicente, V., Simis, S.G.H., Alegre, R., Land, P.E., Groom, S.B., 2013. Above-water reflectance for the evaluation of adjacency effects in earth observation data: initial results and methods comparison for near-coastal waters in the Western Channel, UK. J. Eur. Opt. Soc. Rapid Publ. 8, 13060. https://doi.org/10.2971/JEOS.2013.13060.
Mobley, C.D., 1999. Estimation of the remote-sensing reflectance from above-surface measurements. Appl. Opt. 38, 7442. https://doi.org/10.1364/ao.38.007442.
Mobley, C.D., 2015. Polarized reflectance and transmittance properties of windblown sea surfaces. Appl. Opt. 54, 4828. https://doi.org/10.1364/AO.54.004828.
Mobley, C.D., Gentili, B., Gordon, H.R., Jin, Z., Kattawar, G.W., Morel, A., Reinersman, P., Stamnes, K., Stavn, R.H., 1993. Comparison of numerical models for computing underwaterlight fields. Appl. Opt. 32, 7484–7504.
Mobley, C.D., Boss, E., Roesler, C., 2022. Hydrolight - Radiative Transfer Theory. Ocean Optics Web Book.
Mouw, C.B., Greb, S., Aurin, D., DiGiacomo, P.M., Lee, Z., Twardowski, M., Binding, C., Hu, C., Ma, R., Moore, T., Moses, W., Craig, S.E., 2015. Aquatic color radiometry remote sensing of coastal and inland waters: challenges and recommendations for future satellite missions. Remote Sens. Environ. 160, 15–30. https://doi.org/10.1016/j.rse.2015.02.001.
Nechad, B., Ruddick, K.G., Park, Y., 2010. Calibration and validation of a generic multisensor algorithm for mapping of total suspended matter in turbid waters. Remote Sens. Environ. 114, 854–866. https://doi.org/10.1016/j.rse.2009.11.022.
Neeley, A.R., Mannino, A., 2018. IOCCG Protocol Series (2018). Inherent Optical Property Measurements and Protocols: Absorption Coefficient, IOCCG Ocean Optics and Biogeochemistry Protocols for Satellite Ocean Colour Sensor Validation. Dartmouth, NS, Canada. https://doi.org/10.25607/OBP-119.
Neukermans, G., Loisel, H., Meriaux, X., Astoreca, R., McKee, D., 2012a. In situ variability of mass-specific beam attenuation and backscattering of marine particles with respect to particle size, density, and composition. Limnol. Oceanogr. 57, 124–144. https://doi.org/10.4319/lo.2011.57.1.0124.
Neukermans, G., Ruddick, K., Loisel, H., Roose, P., 2012b. Optimization and quality control of suspended particulate matter concentration measurement using turbidity measurements. Limnol. Oceanogr. Methods 10, 1011–1023. https://doi.org/10.4319/lom.2012.10.1011.
Pan, B., Yu, H., Cheng, H., Du, S., Cai, S., Zhao, M., Du, J., Xie, F., 2023. A CNN–LSTM machine-learning method for estimating particulate organic carbon from remote sensing in lakes. Sustainability (Switzerland) 15. https://doi.org/10.3390/su151713043.
Pavelsky, T.M., Smith, L.C., 2009. Remote sensing of suspended sediment concentration, flow velocity, and lake recharge in the Peace-Athabasca Delta, Canada. Water Resour. Res. 45, 1–16. https://doi.org/10.1029/2008WR007424.
Perez, B.C., Day, J.W., Rouse, L.J., Shaw, R.F., Wang, M., 2000. Influence of Atchafalaya River discharge and winter frontal passage on suspended sediment concentration and flux in Fourleague Bay, Louisiana. Estuar. Coast. Shelf Sci. 50, 271–290. https://doi.org/10.1006/ecss.1999.0564.
Renosh, P.R., Doxaran, D., De Keukelaere, L., Gossn, J.I., 2020. Evaluation of atmospheric correction algorithms for sentinel-2-MSI and sentinel-3-OLCI in highly turbid estuarine waters. Remote Sens. 12 https://doi.org/10.3390/RS12081285.
Roesler, C.S., Barnard, A.H., 2013. Optical proxy for phytoplankton biomass in the absence of photophysiology: rethinking the absorption line height. Methods Oceanogr. 7, 79–94. https://doi.org/10.1016/j.mio.2013.12.003.
Ruddick, K.G., de Cauwer, V., Park, Y.J., Moore, G., 2006. Seaborne measurements of near infrared water-leaving reflectance: the similarity spectrum for turbid waters. Limnol. Oceanogr. 51, 1167–1179. https://doi.org/10.4319/lo.2006.51.2.1167.
Saintilan, N., Kovalenko, K.E., Guntenspergen, G., Rogers, K., Lynch, J.C., Cahoon, D.R., Lovelock, C.E., Friess, D.A., Ashe, E., Krauss, K.W., Cormier, N., Spencer, T., Adams, J., Raw, J., Ibanez, C., Scarton, F., Temmerman, S., Meire, P., Maris, T., Thorne, K., Brazner, J., Chmura, G.L., Bowron, T., Gamage, V.P., Cressman, K., Endris, C., Marconi, C., Marcum, P., Laurent, K., Reay, W., Raposa, K.B., Garwood, J. A., Khan, N., 2022. Constraints on the adjustment of tidal marshes to accelerating sea level rise. Science 1979 (377), 523–527. https://doi.org/10.1126/SCIENCE.ABO7872.
Salter, G., Passalacqua, P., Wright, K., Feil, S., Jensen, D., Simard, M., Lamb, M.P., 2022. Spatial patterns of deltaic deposition/erosion revealed by Streaklines extracted from remotely-sensed suspended sediment concentration. Geophys. Res. Lett. 49 https://doi.org/10.1029/2022GL098443.
Sathyendranath, S., 2000. IOCCG. Remote Sensing of Ocean Colour in Coastal , and Other Optically-Complex, Waters. Reports and Monographs of the International OceanColour Coordinating Group, Dartmouth, NS, Canada.
Savitzky, A., Golay, M.J.E., 1964. Smoothing and differentiation. Anal. Chem. 36, 1627–1639.
Schartau, M., Riethmüller, R., Flöser, G., van Beusekom, J.E.E., Krasemann, H., Hofmeister, R., Wirtz, K., 2019. On the separation between inorganic and organic fractions of suspended matter in a marine coastal environment. Prog. Oceanogr. 171, 231–250. https://doi.org/10.1016/j.pocean.2018.12.011.
Shaw, J.B., Ayoub, F., Jones, C.E., Lamb, M.P., Holt, B., Wagner, R.W., Coffey, T.S., Chadwick, J.A., Mohrig, D., 2016. Airborne radar imaging of subaqueous channel evolution in Wax Lake Delta, Louisiana, USA. Geophys. Res. Lett. 43, 5035–5042. https://doi.org/10.1002/2016GL068770.
Shi, W., Wang, M., 2019. Characterization of suspended particle size distribution in global highly turbid waters from VIIRS measurements. J. Geophys. Res. Oceans 124, 3796–3817. https://doi.org/10.1029/2018JC014793.
Shields, M.R., Bianchi, T.S., Kolker, A.S., 2019. Factors controlling storage, sources, and diagenetic state of organic carbon in a prograding subaerial delta: Wax Lake Delta, Louisiana. J. Geophys. Res. Biogeosci. 1115–1131 https://doi.org/10.1029/2018JG004683.
Slade, W.H., Boss, E., 2015. Spectral attenuation and backscattering as indicators of average particle size. Appl. Opt. 54, 7264. https://doi.org/10.1364/ao.54.007264.
Son, Y.B., Gardner, W.D., Mishonov, A.V., Richardson, M.J., 2009. Multispectral remote-sensing algorithms for particulate organic carbon (POC): the Gulf of Mexico. Remote Sens. Environ. 113, 50–61. https://doi.org/10.1016/j.rse.2008.08.011.
Stramski, D., Babin, M., Woźniak, S.B., 2007. Variations in the optical properties of terrigenous mineral-rich particulate matter suspended in seawater. Limnol. Oceanogr. 52, 2418–2433. https://doi.org/10.4319/lo.2007.52.6.2418.
Stramski, D., Reynolds, R.A., Kaczmarek, S., Uitz, J., Zheng, G., 2015. Correction of pathlength amplification in the filter-pad technique for measurements of particulate absorption coefficient in the visible spectral region. Appl. Opt. 54, 6763. https://doi.org/10.1364/ao.54.006763.
Stramski, D., Joshi, I., Reynolds, R.A., 2022. Ocean color algorithms to estimate the concentration of particulate organic carbon in surface waters of the global ocean in support of a long-term data record from multiple satellite missions. Remote Sens. Environ. 269, 112776 https://doi.org/10.1016/j.rse.2021.112776.
Swarzenski, C.M., 1996. Surface-Water Hydrology of the Gulf Intracoastal Waterway in.
Sweet, J.A., Bargu, S., Morrison, W.L., Parsons, M., Pathare, M.G., Roberts, B.J., Soniat, T.M., Stauffer, B.A., 2022. Phytoplankton dynamics in Louisiana estuaries: building a baseline to understand current and future change. Mar. Pollut. Bull. 175, 113344 https://doi.org/10.1016/j.marpolbul.2022.113344.
Syvitski, J.P.M., Kettner, A.J., Overeem, I., Hutton, E.W.H., Hannon, M.T., Brakenridge, G.R., Day, J., Vörösmarty, C., Saito, Y., Giosan, L., Nicholls, R.J., 2009. Sinking deltas due to human activities. Nat. Geosci. 2, 681–686. https://doi.org/10.1038/ngeo629.
Thompson, D.R., Cawse-Nicholson, K., Erickson, Z., Fichot, C.G., Frankenberg, C., Gao, B. C., Gierach, M.M., Green, R.O., Jensen, D., Natraj, V., Thompson, A., 2019. A unified approach to estimate land and water reflectances with uncertainties for coastal imaging spectroscopy. Remote Sens. Environ. 231 https://doi.org/10.1016/j.rse.2019.05.017.
Thompson, D.R., Jensen, D.J., Chapman, J.W., Simard, M., Greenberg, E., 2023. Delta-X: AVIRIS-NG BRDF-Adjusted Surface Reflectance, MRD, LA, 2021, V2. https://doi.org/10.3334/ORNLDAAC/2139.
Törnqvist, T.E., Jankowski, K.L., Jankowski, K.L., Li, Y.X., Li, Y.X., González, J.L., González, J.L., 2020. Tipping points of Mississippi Delta marshes due to accelerated sea-level rise. Sci. Adv. 6 https://doi.org/10.1126/SCIADV.AAZ5512.
Tran, T.K., Duforêt-Gaurier, L., Vantrepotte, V., Ferreira Jorge, D.S., Mériaux, X., Cauvin, A., d'Andon, F., Loisel, H., 2019. Deriving particulate organic carbon in coastal waters from remote sensing: inter-comparison exercise and development of a maximum band-ratio approach. Remote Sens. 11 https://doi.org/10.3390/rs11232849.
Trefry, J.H., Metz, S., Nelsen, T.A., Trocine, R.P., Eadie, J., Eadie, B.J., 1994. Transport of particulate organic carbon by the Mississippi River and its fate in the Gulf of Mexico. Estuaries 17, 839–849.
Twilley, R.R., Bentley, S.J., Chen, Q., Edmonds, D.A., Hagen, S.C., Lam, N.S.N., Willson, C.S., Xu, K., Braud, D.W., Hampton Peele, R., McCall, A., 2016. Co-evolution of wetland landscapes, flooding, and human settlement in the Mississippi River Delta Plain. Sustain. Sci. 11, 711–731. https://doi.org/10.1007/s11625-016-0374-4.
Vandermeulen, R.A., Mannino, A., Neeley, A., Werdell, J., Arnone, R., 2017. Determining the optimal spectral sampling frequency and uncertainty thresholds for hyperspectral remote sensing of ocean color. Opt. Express 25, A785. https://doi.org/10.1364/oe.25.00a785.
Verma, N., Lohrenz, S., Chakraborty, S., Fichot, C.G., 2021. Underway hyperspectral bio-optical assessments of phytoplankton size classes in the river-influenced northern Gulf of Mexico. Remote Sens. 13, 3346. https://doi.org/10.3390/RS13173346.
Wang, X.C., Chen, R.F., Gardner, G.B., 2004. Sources and transport of dissolved and particulate organic carbon in the Mississippi River estuary and adjacent coastal waters of the northern Gulf of Mexico. Mar. Chem. 89, 241–256. https://doi.org/10.1016/j.marchem.2004.02.014.
Welch, H.L., Coupe, R.H., Aulenbach, B.T., 2014. National stream quality accounting network concentrations and transport of suspended sediment, nutrients, and pesticides in the lower Mississippi-Atchafalaya River subbasin during the 2011 Mississippi River flood, April through July scientific Investigati. U.S. Geol. Surv. Sci. Investig. Rep. 2014–5100, 1–44.
Werdell, J.P., McKinna, L.I.W., Boss, E., Ackleson, S.G., Craig, S.E., Gregg, W.W., Lee, Z., Maritorena, S., Roesler, C.S., Rousseaux, C.S., Stramski, D., Sullivan, J.M., Twardowski, M.S., Tzortziou, M., Zhang, X., 2018. An overview of approaches and

challenges for retrieving marine inherent optical properties from ocean color remote sensing. Prog. Oceanogr. https://doi.org/10.1016/j.pocean.2018.01.001.

Wold, S., Sjöström, M., Eriksson, L., 2001. PLS-regression: A basic tool of chemometrics. Chemom. Intell. Lab. Syst. 58, 109–130. https://doi.org/10.1016/S0169-7439(01)00155-1.

Woźniak, S.B., Stramski, D., Stramska, M., Reynolds, R.A., Wright, V.M., Miksic, E.Y., Cichocka, M., Cieplak, A.M., 2010. Optical variability of seawater in relation to particle concentration, composition, and size distribution in the nearshore marine environment at Imperial Beach, California. J. Geophys. Res. Oceans 115, 1–19. https://doi.org/10.1029/2009JC005554.

Woźniak, S.B., Darecki, M., Zabłocka, M., Burska, D., Dera, J., 2016. New simple statistical formulas for estimating surface concentrations of suspended particulate matter (SPM) and particulate organic carbon (POC) from remote-sensing reflectance in the southern Baltic Sea. Oceanologia 58, 161–175. https://doi.org/10.1016/j.oceano.2016.03.002.

Wright, K., Passalacqua, P., Simard, M., Jones, C.E., 2022. Integrating connectivity into hydrodynamic models: an automated open-source method to refine an unstructured mesh using remote sensing. J. Adv. Model. Earth Syst. 14 https://doi.org/10.1029/2022MS003025.

Xu, Jie, Lei, S., Bi, S., Li, Y., Lyu, H., Xu, Jiafeng, Xu, X., Mu, M., Miao, S., Zeng, S., Zheng, Z., 2020. Tracking spatio-temporal dynamics of POC sources in eutrophic lakes by remote sensing. Water Res. 168, 115162 https://doi.org/10.1016/j.watres.2019.115162.

Zhang, X., Hu, L., 2009. Scattering by pure seawater at high salinity. Opt. Express 17, 12685. https://doi.org/10.1364/oe.17.012685.

Zhang, X., He, S., Shabani, A., Zhai, P.-W., Du, K., 2017. Spectral Sea surface reflectance of skylight. Opt. Express 25, A1. https://doi.org/10.1364/oe.25.0000a1.

Zhang, X., Fichot, C.G., Baracco, C., Guo, R., Neugebauer, S., Bengtsson, Z., Ganju, N., Fagherazzi, S., 2020. Determining the drivers of suspended sediment dynamics in tidal marsh-influenced estuaries using high-resolution ocean color remote sensing. Remote Sens. Environ. 240, 111682 https://doi.org/10.1016/j.rse.2020.111682.